Journal of Control Science and Engineering

Advanced Optimization Techniques for Operation and Control of Intelligent Power Systems

Lead Guest Editor: Hassan Haes Alhelou
Guest Editors: Baseem Khan and Pawan Singh

Advanced Optimization Techniques for Operation and Control of Intelligent Power Systems

Journal of Control Science and Engineering

Advanced Optimization Techniques for Operation and Control of Intelligent Power Systems

Lead Guest Editor: Hassan Haes Alhelou
Guest Editors: Baseem Khan and Pawan Singh

Contents

Hindawi
Journal of Control Science and Engineering
Volume 2020, Article ID 8896612, 8 pages
https://doi.org/10.1155/2020/8896612

Research Article

Beetle Swarm Optimization Algorithm-Based Load Control with Electricity Storage

Hengjing He,[1] Shangli Zhou,[1] Leping Zhang,[1] Junhong Lin,[1] Weile Chen,[2] and Di Wu[2]

[1]*Digital Grid Research Institute, CSG, Guangzhou 510663, China*
[2]*School of Electrical Engineering and Automation, Hefei University of Technology, Hefei 230009, China*

Correspondence should be addressed to Di Wu; wudi1107@mail.hfut.edu.cn

Received 31 August 2020; Revised 27 October 2020; Accepted 9 November 2020; Published 25 November 2020

Academic Editor: Hassan Haes Alhelou

Based on the intelligent bidirectional interactive technology, this paper studies the flexible working mode and optimal power consumption strategy of several typical power consumption loads including energy storage equipment. Based on the real-time price scheme, the objective function and constraints are obtained, and the adaptive algorithm for beetle swarm optimization with variable whisker length is used to optimize so that the electric equipment can automatically change its power load through the intelligent terminal and even work in the way of reverse power transmission. The proposed optimal scheduling algorithm can not only maximize the interests of users but also ensure the minimum peak to average ratio so as to realize peak shaving and valley filling. Simulation results verify the effectiveness of the algorithm.

1. Introduction

With the continuous increase in power demand and the deepening of power market reform, the demand side management (DSM) based on orderly power consumption is more and more adopted by power grid enterprises [1]. However, the traditional orderly power consumption management, no matter what kind of technology, or by imposing restrictions on the user's power load in a certain period of time, or through the electricity price incentive policy to let the user limit the power consumption load in a certain period of time, for a single power consumption equipment, is rigid to participate in the peak shaving and valley filling of the power grid in the way of work or outage. This traditional and mandatory DSM model often leads to the lack of flexibility in the electricity market, which deepens the interest conflict between the supply side and the demand side.

In order to solve the shortage of power supply and reduce the load peak valley difference, an effective way is used to increase the elasticity of power demand and introduce a competition mechanism on the power demand side. The demand side is no longer the traditional and passive receiver but can respond according to the price signal or incentive mechanism, actively change the demand of electricity, participate in the power management, and obtain corresponding benefits, namely, demand response (DR) [2]. Different from the traditional and passive DSM mode, intelligent DSM adopts intelligent bidirectional interaction technology. With the access of intelligent terminal equipment, the development of power communication technology, and the increase in the proportion of intelligent controllable load in the family, the intelligent two-way interactive technology of power consumption becomes possible [3]. The two-way interaction technology provides a technical basis for residents to participate in automatic demand response and realize intelligent power consumption. It can not only effectively improve the utilization rate of electric energy and the operation efficiency of the power grid but also achieve the purpose of maintaining the stability and reliability of the power system and market.

The theory of demand-side management (DSM) has been developed for decades in the world [4]. However, it was not until the blackout in California in 2001 that many countries paid attention to and developed DSM based on the market. Compared with developed countries in Europe and

America, the development of intelligent electricity technology and theory in China is relatively slow. Song [5] first introduces the concept and implementation principles of demand-side response and the implementation plan of demand response in the United States. Then, Zhang et al. [6] give a comprehensive introduction to the demand side response in combination with the actual situation in China and give relevant suggestions and assumptions.

In order to solve the specific automation demand response technology, various software and hardware design schemes have been proposed, such as the software and hardware design and implementation scheme of the user side energy management prototype system [7], the management and control scheme of smart appliances based on user comfort [3], the massive data storage problem of smart grid based on Hadoop cloud computing platform [8], and the designer of smart grid two-way interactive platform system case [9]. In addition, how to optimize the load regulation and control algorithm has been proposed constantly, such as the residential user power dispatching strategy based on the price forecasting scheme [10], the user power dispatching strategy based on the noncooperative game method [11], simulated annealing-based krill herd algorithm [12], multiobjective optimization method based on adaptive parameter harmony search algorithm [13], and improved quantum-behaved particle swarm optimization with elitist breeding [14]. In the work [15], the particle swarm optimization (PSO) algorithm is employed to handle the PSP and to obtain an optimal smart home appliances schedule. The work in [16] presents two bio-inspired energy optimization techniques, i.e., the grasshopper optimization algorithm (GOA) and bacterial foraging algorithm (BFA), for power scheduling in a single office. In order to solve the problem of instability and high-cost of photovoltaic power generation, the optimal scheduling model of a photovoltaic power system was established by minimizing power generation scheduling cost. The model increases the ability of load controlling by virtue of the demand response of price to reduce the influence of the instability of photovoltaic generation on optimal scheduling results. For solving the model, the classical genetic algorithm was improved [17]. In a deregulated electricity market, the power system operator should systematically identify the optimal schedule of renewable distributed generation (DG) units to not only optimize the market profits but also to improve the network conditions. The work in [18] proposes a parallel computation-based methodology using fuzzy logic designed in the structure of a genetic algorithm (GA). A large number of electric vehicles (EV) connected to the grid will affect the planning and operation of the power system. Hence, it is of great significance to guide the charging behavior of electric vehicles in an orderly manner. Regarding this kind of problem, an electric vehicle intelligent charging navigation strategy based on real-time electricity price is proposed, where the PSOGA algorithm is used to solve the optimal scheme. The motivation is to guide the EV charging towards an orderly way by virtue of the real-time electricity price mechanism [19].The work in [20] compares the effects of different optimization algorithms for different reference functions. However, the energy storage equipment is not considered in these scheduling strategies, and the scheduling scheme is only given from the distribution side or the user side.

In this paper, based on the intelligent electricity bidirectional interaction technology, the flexible working mode and power consumption strategy of several typical electrical loads including energy storage equipment are studied. Based on the real-time price scheme, the optimal scheduling algorithm is given so that the power consumption equipment can automatically change its power load through the intelligent terminal and even work in the way of reverse power transmission. By using the adaptive algorithm for beetle swarm optimization with variable whisker length, i can not only maximize the interests of users but also ensure the minimum peak to average ratio, so as to realize peak shaving and valley filling. Firstly, the mathematical modeling of several typical loads is carried out; then, based on the real-time price scheme, the optimization objective function is given, which includes two parts: one is the user's electricity cost, and the other is the peak to average ratio. Finally, the optimal control algorithm is given, and an example is analyzed.

2. Intelligent Bidirectional Interactive Operation of the Smart Grid

2.1. System Description. In the traditional orderly power consumption management, for residential users, either through the peak load regulation strategy of forced switching off or through the price incentive policy, users can limit their power consumption load in a certain period of time. For users, it is basically in a passive state of power consumption. In order to mobilize users to change their electricity demand actively and participate in power consumption management, intelligent two-way interactive technology is more and more adopted. Its interaction model is shown in Figure 1. According to the total load, the power supply side issues the price signal in real time, and the user side makes demand response according to the real-time price signal, so as to achieve the purpose of maximizing the interests of users and smoothing the load curve of the grid. Due to the lack of professional knowledge of residents, it is inconvenient to participate in demand response. In order to not affect the normal life of residents and let more users participate in the demand response, the development of intelligent terminal equipment, the realization of intelligent management of household appliances, and the automatic control of demand response are the important contents of realizing intelligent power consumption. In order to realize intelligent power consumption, it is very important to design the optimal dispatching algorithm of power load based on the characteristics of the typical load.

2.2. Classification of Household Electricity Load. In order to facilitate the analysis and calculation, the user power load is divided into three categories:

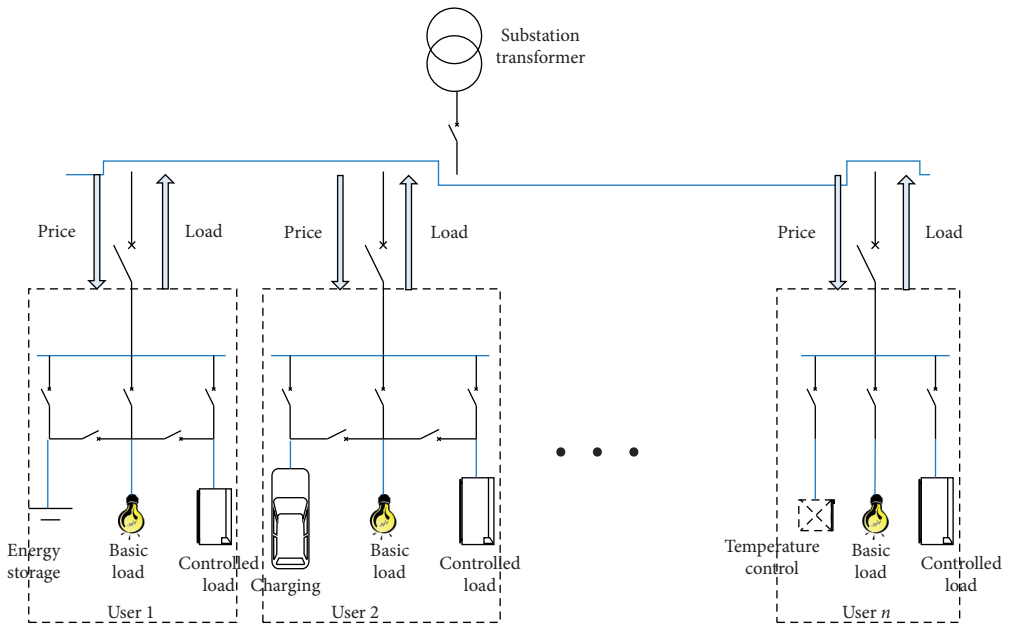

Figure 1: Intelligent bidirectional interactive operation model.

(i) α-type dynamic load: the controllable load that can be completely scheduled in the dispatching time. The total load in the dispatching time is unchanged and has the function of reverse power transmission, such as energy storage equipment and electric vehicle; the set of such electrical equipment is marked as U_α.

(ii) β-type dynamic load: the controllable load that can be completely scheduled within the dispatching time is the same as the total load within the dispatching time, but it does not have the function of reverse power transmission, such as temperature control equipment and water heater; the set of such electrical equipment is marked as U_β.

(iii) γ-type dynamic load: for the load fixed in the dispatching time, such as lighting equipment and television, the set of such electrical equipment is marked as U_γ; all consumers are marked as U.

2.3. Real-Time Electricity Price. In order to realize fair power consumption and peak load shifting, it is an effective means to adopt the real-time electricity price strategy by citing the competition mechanism. Without losing generality, it is assumed that there are n users participating in intelligent power consumption, and all users' electrical equipment is recorded as a set $\Gamma = \{1, 2, \ldots, N\}$. Considering that many electric loads do not work in a complete small period of time ΔT, each hour can be divided into several equal time periods, so each hour period can be divided into $L = (1/\Delta T)$. Without losing generality, let L be an integer. Then, the whole day from 0:00 to 24:00 can be divided into $H = 24L$ segments, denoted as $M = \{1, 2, \ldots, H\}$. The time period $i \in M$ represents the time period area $[i-1, i] \cdot \Delta T$.

For any device $j \in \Gamma$, it is assumed that the load over the time period $i \in M$ is a constant l_j^i and written as a vector; $l_j = [l_j^1, \ldots, l_j^H]$, $j \in \Gamma$, indicates the load j in the whole day. Let $L_i = \sum_{j \in \Gamma} l_j^i$ be the sum of all user loads above the time period $i \in M$.

For a substation transformer, the total electricity charge can be determined in sections according to the current total load. When the power consumption does not exceed the basic load, the electricity price is relatively low. When the power consumption exceeds the basic load, the high price is adopted, such as the simple piecewise linear function as follows:

$$E_i(L_i) = \begin{cases} a_i L_i, & 0 \le L_i \le L_i^*, \\ a_i L_i^* + b_i (L_i - L_i^*), & L_i \ge L_i^*, \\ 0 < a_i \le b_i, \end{cases} \tag{1}$$

where is the corresponding constant of a_i, b_i, L_i^* and can be adjusted according to the time calculation. As mentioned in [11], the parameters adopted by a Canadian power company are as follows:

$$\begin{aligned} a_i &= 5.9\,\text{c/kWh}, \\ b_i &= 8.3\,\text{c/kWh}, \\ L_i^* &= 24\,\text{kWh}. \end{aligned} \tag{2}$$

According to the total electricity charge, the station transformer charges the equipment j the electricity fee according to the proportion: $e_j^i = (l_j^i / L_i) E_i(L_i)$, where l_j^i is the electrical load of i^{th} period of load j. From the point of view of a single user, it is hoped that the single consumption will be the lowest; that is, it is hoped that e_j^i will be the smallest, while from the point of view of the whole station change, it is hoped that $E_i(L_i)$ will be kept the smallest.

In addition, as the power supplier, we hope that the peak valley difference is the minimum. The peak load is defined as $L_{\text{peak}} = \max_{i \in M} L_i$; the average load is $L_{\text{avg}} = (1/H) \sum_{i=1}^{H} L_i$, and the peak to average ratio is,

$$\text{PAR} = \frac{L_{\text{peak}}}{L_{\text{avg}}}. \tag{3}$$

For a whole day's electric load, the average value of the load is usually constant. Therefore, as the power supply side, it is necessary to ensure that the peak to average ratio reaches the minimum value.

2.4. Participation of Energy Storage Equipment in Generation Subsidy Price. In order to solve the problem of insufficient power supply, an effective way is to encourage users to use energy storage equipment (such as energy storage battery and electric vehicle) to discharge during peak load. Therefore, the electricity price subsidy policy is adopted, and the traditional electricity price subsidy policy adopts the unified subsidy price, which is a lack of flexibility. Therefore, the subsidy tariff can be formulated according to the load at the current moment. For example, the following subsidy function can be simply used:

$$S_i(L_i, Q_i) = \begin{cases} c_i L_i Q_i, & L_i \geq L_i^{**}, \\ 0, & \end{cases} \tag{4}$$

where c_i is a constant, L_i^{**} is the corresponding constant, L_i is the total load at the current time, and Q_i is the total discharge load at the current time, which is recorded as a negative value. Obviously, if the current total load is large and higher than the set critical value L_i^{**}, the energy storage equipment is encouraged to participate in power generation and subsidize the electricity charge; on the contrary, if the current total load is small and lower than the set threshold L_i^{**}, the power supply is sufficient and the users are not encouraged to participate in power generation. For the convenience of mathematical description, the total discharge load Q_i can be expressed as $Q_i = \sum_{j \in \Gamma} g(l_j^i)$:

$$g\left(l_j^i\right) = \begin{cases} l_j^i, & l_j^i < 0, \\ 0, & l_j^i \geq 0. \end{cases} \tag{5}$$

3. Optimal Orderly Operation Control Algorithm of Power Load

Based on the above mathematical description, taking the minimum cost and peak to average ratio as the optimization objectives and taking the load of each power consumption equipment and each period as the control object, the optimization objective function is,

$$\begin{aligned} \min f\left(l_j^i\right) &= \sum_{i=1}^{H} \left(E_i(L_i) + S_i(L_i, Q_i)\right) + \lambda \cdot \text{PAR} \\ &= \sum_{i=1}^{H} \left(E_i\left(\sum_{j \in \Gamma} l_j^i\right) + S_i\left(\sum_{j \in \Gamma} l_j^i, \sum_{j \in \Gamma} g\left(l_j^i\right)\right)\right) \\ &\quad + \frac{\lambda}{L_{\text{avg}}} \cdot \max_{i \in M} \sum_{j \in \Gamma} l_j^i, \end{aligned} \tag{6}$$

where λ is the weighting factor, $S_i(L_i, Q_i)$ is the subsidy function, and PAR is the peak to average ratio.

The following statements are to analyze the constraint conditions: for any equipment j, $i_{s,j}$ is used to indicate the start time of load dispatching, $i_{e,j}$ is the end time of load dispatching, and the total load of electric load in the whole dispatching time is fixed, which is recorded as a constant value P_j, i.e., $\sum_{i=i_{s,j}}^{i=i_{e,j}} l_j^i = P_j$. The load device does not work outside the dispatch time, $l_j^i = 0$, $0 \leq i < i_{s,j}, i_{e,j} < i \leq H$.

In addition, for any electrical equipment, its load generally has upper and lower limits, that is, $l_j^{\min} \leq l_j^i \leq l_j^{\max}$. If the load is negative, it indicates the discharge state. Therefore, the general constraint is,

$$\Omega_1 = \left\{ l_j^i, \quad i \in M,\ j \in \Gamma \,\middle|\, \sum_{i=i_{s,j}}^{i=i_{e,j}} l_j^i = P_j, \quad l_j^i = 0,\ 0 \leq i < i_{s,j}, i_{e,j} < i \leq H,\ l_j^{\min} \leq l_j^i \leq l_j^{\max} \right\}. \tag{7}$$

From the optimization point of view, the total load in a day should remain unchanged; that is, the optimization function L_{avg} is constant, and the specific value is,

$$L_{\text{avg}} = \sum_{j \in \Gamma} \frac{P_j}{H}. \tag{8}$$

In addition, the objective optimization function contains a maximum function, which is not conducive to find the optimal value. The method of adding a variable can be used. For example, if the variable ρ is used, then the objective function (6) can be expressed as,

$$\min f\left(l_j^i\right) = \sum_{i=1}^{H}\left(E_i\left(\sum_{j\in\Gamma} l_j^i\right) + S_i\left(\sum_{j\in\Gamma} l_j^i, \sum_{j\in\Gamma} g\left(l_j^i\right)\right)\right) + \frac{\lambda H}{\sum_{j\in\Gamma} P_j}\cdot\rho. \tag{9}$$

By adding the constraint conditions, we get,

$$\Omega_2 = \left\{ l_j^i, \quad i\in M,\ j\in\Gamma \,\middle|\, \sum_{j\in\Gamma} l_j^i \le \rho \right\}, \tag{10}$$

which implies that the final constraint is $\Omega_1 \cap \Omega_2$.

4. Adaptive Algorithm for Beetle Swarm Optimization with Variable Whisker Length

We first introduce the beetle antennae search (BAS) algorithm and then beetle swarm optimization (BSO). The main difference is that the former is based on a single individual, and the latter is based on multiple individuals.

4.1. Principle of Beetle Antennae Search Algorithm. In the beetle antennae search (BAS) algorithm, we now use the following two rules inspired by the behavior of beetle searching with antennae, which includes searching behavior and detecting behavior. It is noted that the beetle searches randomly to explore an unknown environment. The specific steps are as follows:

Step 1: assume that the position of longicorn beetles in n-dimensional solution space is $X = (x_1, x_2, \ldots, x_n)$, to model the searching behavior, and we propose describing a random direction of beetle searching as follows:

$$\overrightarrow{p} = \frac{\text{rand}(n,1)}{\|\text{rand}(n,1)\|}, \tag{11}$$

where $\text{rand}(n,1)$ is an n-dimensional vector of random numbers in the range of $(0,1)$.

Step 2: we present the searching behaviors of both right-hand and left-hand sides, respectively, to imitate the activities of the beetle's antennae:

$$\begin{cases} x_l^k = x^k - \mathrm{d}\overrightarrow{p}, \\ x_r^k = x^k + \mathrm{d}\overrightarrow{p}, \end{cases} \tag{12}$$

where x^k is the current position of longicorn beetles, d is the distance from the center of mass to the antennae, x_r^k denotes a position lying in the searching area of the right-hand side, and x_l^k denotes that of the left-hand side.

Step 3: location update method:

$$x^{k+1} = x^k + \overrightarrow{p}\,\delta^k \text{sign}\left(f\left(x_l^k\right) - f\left(x_r^k\right)\right), \tag{13}$$

where δ^k is the current step size, sign is a symbolic function, and f is the function to be optimized.

4.2. Principle of Particle Swarm Optimization (PSO) Algorithm. The basic concept of the PSO algorithm is that individuals in a group share information, so that the movement of the whole group can change from disorder to order in the process of solving problems, and finally, the best solution to the problem can be obtained. The specific steps are as follows:

Step 1: suppose that the population size of particle swarm optimization in n-dimensional solution space is N, and the coordinate position vector of each particle is expressed as $X_i = (x_{i1}, x_{i2}, \ldots, x_{in})$.

The velocity vector of each particle is expressed as $V_i = (v_{i1}, v_{i2}, \ldots, v_{in})$. The optimal position of an individual is expressed as $P_i = (p_{i1}, p_{i2}, \ldots, p_{in})$, and the optimal position of the population is $P_m = (p_{m1}, p_{m2}, \ldots, p_{mn})$.

Step 2: in the k-th iteration, the position and velocity of the d-dimension of the i-th particle are updated as follows:

$$\begin{cases} v_{\text{id}}^{k+1} = \omega v_{\text{id}}^k + c_1\,\text{rand}\left(P_{\text{id}}^k - x_{\text{id}}^k\right) \\ +c_2\,\text{rand}\left(p_{md}^k - x_{\text{id}}^k\right), \\ x_{\text{id}}^{k+1} = x_{\text{id}}^k + v_{\text{id}}^{k+1}, \end{cases} \tag{14}$$

where w is the inertia weight, c_1 and c_2 are learning factors and rand random numbers in the range of $(0,1)$.

Step 3: the particle optimal position updating method is as follows:

$$P_i^{k+1} = \begin{cases} X_i^{k+1}, f\left(X_i^{k+1}\right) < f\left(P_i^k\right), \\ P_i^k, f\left(X_i^{k+1}\right) \ge f\left(P_i^k\right), \end{cases} \tag{15}$$

where f is the function to be optimized.

4.3. Principle of Particle Swarm Optimization Algorithm Based on Beetle Antennae Search. There are many unknown parameters in the optimization scheduling system model studied in this paper. In this paper, a particle swarm optimization algorithm (BSO) based on a longicorn whisker search is proposed based on the idea of the BAS algorithm and PSO algorithm. The initial position and velocity process of the beetle antennae algorithm are consistent with that of PSO. However, due to the lack of local information acquisition around the current particle individual in the evolutionary direction strategy of PSO, it is unstable and prone to local optimal solution in the case of multidimensional complexity. The BSO proposed in this paper uses the idea of beetle antennae search and has its own judgment on the environment space in each iteration process; that is, individuals compare the fitness function values of left and right whiskers in each iteration and compare the values of

the two. Through this method, the adaptive problems of different groups and iterative stages can be improved, and the instability and local optimal solution problems of the algorithm are solved. The specific steps are as follows:

Step 1: suppose that the population size of longicorn beetle population in n-dimensional space and the standardized direction vector generated by each individual are

$$\overrightarrow{p}_i = \frac{\text{rand}(n,1)}{\|\text{rand}(n,1)\|}. \tag{16}$$

According to the relationship between the optimal position of the group and the optimal position distance of the individual, the distance between the left and right whiskers of the i-th longicorn in the k-th iteration is calculated as follows:

$$d_i^k = \beta \|P_m - P_i\|. \tag{17}$$

Step 2: according to the fitness function of the left and right sides of an individual, by comparing the values on both sides, the speed generated by the fitness of each individual in the population is updated as follows:

$$\Delta v_i = \overrightarrow{p}_i \,\text{sign}\left(f\left(x_{il}^k\right) - f\left(x_{ir}^k\right)\right). \tag{18}$$

Step 3: in the k-th iteration, the velocity and position of the i-th individual are updated as follows:

$$\begin{aligned} V_i^{k+1} &= \omega V_i^k + c_1 \,\text{rand} \cdot \left(P_i^k - X_i^k\right) + c_2 \,\text{rand} \cdot \left(P_m^k - X_i^k\right) \\ &\quad + d_i^k \,\text{rand} \cdot \overrightarrow{p}_i \,\text{sign}\left(f\left(x_{il}^k\right) - f\left(x_{ir}^k\right)\right), \\ X_i^{k+1} &= X_i^k + V_i^{k+1}, \end{aligned} \tag{19}$$

where w is the inertia weight and c_1 and c_2 is the learning factor and the matrix dot multiplication represents the multiplication of corresponding elements of the same type matrix.

Step 4: after completing the iteration process, the global optimal solution can be obtained.

5. Simulation Results

It is considered that there are three household users participating in intelligent power consumption under a substation transformer, and each user has three different types of power load (see Table 1 for details). If a smaller resolution is adopted, different parameter L can be selected to obtain more accurate results, but it will bring a certain computational burden. For simplicity, the day is divided into 24 small periods, i.e., $L = 1$.

The electricity charge is collected by piecewise function (1), where the parameter is $a_i = 0.5$, $b_i = 0.8$, and $L_i^* = 2.5$. If reverse generation is used, the subsidy tariff is calculated according to function (4), where the parameter is $c_i = 0.2$ and $L_i^{**} = 2$.

For comparison, first, it is considered that all users do not participate in intelligent power consumption and power generation. Under the premise of no loss of generality, the load is assumed to be uniformly distributed during the scheduling time; for α-type dynamic load, the load is evenly distributed within the dispatching time, while for β-type dynamic load, the load is evenly distributed within the dispatching time and does not participate in power generation. Actually, there is no difference between α-type and β-type dynamic load in this case. By a simple calculation, Figure 2 shows the power load of each time period in this case.

Through the formula

$$\begin{aligned} E_i(L_i) &= \begin{cases} a_i L_i, & 0 \le L_i \le L_i^*, \\ a_i L_i^* + b_i\left(L_i - L_i^*\right), & L_i \ge L_i^*,\ 0 < a_i \le b_i, \end{cases} \\ \text{PAR} &= \frac{L_{\text{peak}}}{L_{\text{avg}}}, \end{aligned} \tag{20}$$

the peak to average ratio is 1.9786, and the total electricity charge is 47.7286.

If the intelligent dispatching optimization control algorithm proposed in this paper is adopted, where $\lambda = 3$, the daily power load is shown in Figure 3.

If the intelligent dispatching optimization control algorithm proposed in this paper is adopted, the power load of one day is shown in Figure 3.

By solving the optimal problem,

$$\begin{aligned} \min f\left(l_j^i\right) &= \sum_{i=1}^{H} \left(E_i\left(\sum_{j\in\Gamma} l_j^i\right) + S_i\left(\sum_{j\in\Gamma} l_j^i, \sum_{j\in\Gamma} g\left(l_j^i\right)\right)\right) \\ &\quad + \frac{\lambda H}{\sum_{j\in\Gamma} P_j} \cdot \rho, \end{aligned} \tag{21}$$

$$\text{PAR} = \frac{L_{\text{peak}}}{L_{\text{avg}}}. \tag{22}$$

According to the calculation, the peak to average ratio is 1.1670, increased by 41.02%; the total electricity charge is 24.2140, including 15.3871 income from power generation, saving 49.27% in total. Therefore, based on the intelligent power consumption strategy, it not only maximizes the interests of users but also effectively participates in peak shaving and valley filling of the power grid.

To have a comparison among different kinds of optimal algorithms for solutions (21) and (22), as shown in Table 2, some popular optimal algorithms are employed: beetle swarm optimization (BSO) algorithm, particle swarm optimization (PSO) algorithm, particle swarm optimization with dynamic adjustment of inertial weights (PSO-w), and beetle antennae search (BAS) algorithm.

In this paper, the mean value of the optimal value, the standard deviation of the optimal value, and the running

Table 1: Electricity load information of all users.

	User 1		User 2		User 3		Load size
γ-type dynamic load	0.5 kWh	0:00 h–24:00 h	1 kWh	0:00 h–24:00 h	1.5 kWh	0:00 h–24:00 h	0~2.5 kWh
	1 kWh	19:00 h–21:00 h	1 kWh	18:00 h–22:00 h	1 kWh	18:00 h–23:00 h	
β-type dynamic load	2 kWh	12:00 h–24:00 h	4 kWh	08:00 h–22:00 h	6 kWh	10:00 h–22:00 h	0~1 kWh
α-type dynamic load	0 kWh	00:00 h–24:00 h	4 kWh	00:00 h–08:00 h 19:00 h–24:00 h	6 kWh	00:00 h–08:00 h 20:00 h–24:00 h	-1 kWh~1 kWh

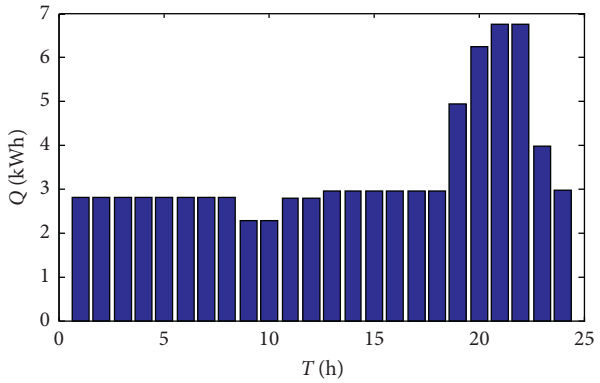

Figure 2: Load without smart use of electricity.

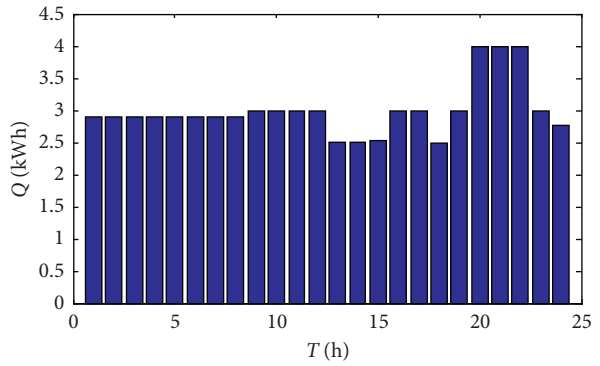

Figure 3: Load under smart use of electricity.

Table 2: Comparison of the convergence speed and accuracy of the algorithm.

Algorithm	Ave.	Std.	t/s
BSO	24.2140	$5.6E-24$	0.51
PSO	25.2469	$5.7E-06$	2.09
PSO-w	25.0300	$1.7E-03$	1.35
BAS	27.4604	$1.22E+00$	3.74

time of the algorithm to complete 1000 iterations are used as the main comparison data. Clearly, the performance of the BSO algorithm is obviously better than BAS and PSO algorithms.

6. Conclusion

Taking residential users participating in intelligent power consumption as an example, this paper considers the optimal scheduling control algorithm of several typical loads including energy storage equipment and proves the superiority of the method based on the adaptive algorithm for beetle swarm optimization with variable whisker length. Based on mathematical modeling, real-time price, and generation subsidy price mechanism, the optimal control model is given. The optimal objective function not only considers the maximization of the user's income but also takes into account the peak valley difference in power load. The proposed algorithm provides a technical basis for the realization of intelligent power consumption and distributed generation. The next step is to study the influence of various parameters on the optimization objectives.

Data Availability

No data were used to support this study.

Conflicts of Interest

The authors declare that there are no conflicts of interest regarding the publication of this paper.

Acknowledgments

No funding is received.

References

[1] W. Wu, J. Pang, G. Chen, and X. Wang, "Research on development of electric power demand side response," *Technology Forum*, vol. 3, pp. 86–94, 2014.

[2] Q. Zhang, X. Wang, M. Fu, and J. Wang, "Smart distribution grid and distribution automation," *Automation of Electric Power System*, vol. 33, no. 17, pp. 49–55, 2009.

[3] Y. Tang, Z. Lu, L. Jia, and Y. Lin, "Management and control scheme for intelligent home appliances based on electricity demand response," *Automation of Electric Power System*, vol. 38, no. 9, pp. 93–99, 2014.

[4] J. Hu, H. Wang, and Z. Zhou, "International experience of power demand side management and enlightenment to China," *Power System Technology*, vol. 31, no. 18, pp. 10–14, 2007.

[5] P. Song, "Application of demand side response in peak load shifting and valley filling in foreign countries," *Shanghai Energy Conservation*, no. 2, pp. 47–50, 2004.

[6] Q. Zhang, X. Wang, J. Wang et al., "Survey of demand response research in deregulated electricity markets," *Automation of Electric Power System*, vol. 32, no. 3, pp. 97–106, 2008.

[7] W. Yang, G. He, and Q. Wang, "Design and implementation of user energy archetype system," *Automation of Electric Power System*, vol. 36, no. 20, pp. 74–79, 2012.

[8] X. Meng and L. Zhou, "Research on resource storage technologies of HDFS for smart grid. Based on hadoop cloud platform," *Electrical Measurement & Instrumentation*, vol. 51, no. 19, pp. 24–30, 2014.

[9] H. Liang, G. Ding, and D. Jiang, "Research and application in smart grid suited user interaction management platform," *Electrical Measurement & Instrumentation*, vol. 49, no. 1, pp. 49–51, 2012.

[10] A.-H. Mohsenian-Rad and A. Leon-Garcia, "Optimal residential load control with price prediction in real-time electricity pricing environments," *IEEE Transactions on Smart Grid*, vol. 1, no. 2, pp. 120–133, 2010.

[11] A.-H. Mohsenian-Rad, V. W. S. Wong, J. Jatskevich, R. Schober, and A. Leon-Garcia, "Autonomous demand-side management based on game-theoretic energy consumption scheduling for the future smart grid," *IEEE Transactions on Smart Grid*, vol. 1, no. 3, pp. 320–331, 2010.

[12] G.-G. Wang, L. Guo, A. H. Gandomi, A. H. Alavi, and H. Duan, "Simulated annealing-based krill herd algorithm for global optimization," *Journal of Control Science and Engineering*, vol. 2013, Article ID 213853, 11 pages, 2013.

[13] P. Sabarinath, M. R. Thansekhar, and R. Saravanan, "Multi-objective optimization method based on adaptive parameter harmony search algorithm," *Journal of Control Science and Engineering*, vol. 2015, Article ID 165601, 12 pages, 2015.

[14] Z.-L. Yang, A. Wu, and H.-Q. Ming, "An improved quantum-behaved particle swarm optimization algorithm with elitist breeding for unconstrained optimization," *Journal of Control Science and Engineering*, vol. 2015, Article ID 326431, 12 pages, 2015.

[15] S. N. Makhadmeh, A. T. Khader, M. A. Al-Betar et al., "Particle swarm optimization algorithm for power scheduling problem using smart battery," in *Proceedings of the 2019 IEEE Jordan International Joint Conference on Electrical Engineering and Information Technology (JEEIT), IEEE, Amman, Jordan*, April 2019.

[16] I. Ullah, Z. Khitab, M. Khan et al., "An efficient energy management in office using bio-inspired energy optimization algorithms," *Processes*, vol. 7, no. 3, 2019.

[17] P. Tingting, L. I. Junxiang, H. Fangjiu et al., "Optimization and algorithm improvement of photovoltaic power system based on demand response," *Journal of University of Shanghai for ENCE and Technology*, vol. 41, no. 5, pp. 448–454, 2019.

[18] P. Okunade, M. Ansari, A. Asrari et al., "Application of optimization for daily scheduling of renewable distributed generations considering market profits in distribution networks," in *Proceedings of the 2018 North American Power Symposium (NAPS), IEEE, Fargo, ND, USA*, September 2018.

[19] W. U. Rui, Z. Liangsong, and Y. Zhandong, "Intelligent charging navigation for electric vehicles based on real-time electricity price," *Electric Power*, vol. 53, no. 4, pp. 131–146, 2020.

[20] T. Wang, L. Yang, and Q. Liu, "Beetle swarm optimization algorithm: theory and application," 2018, https://arxiv.org/abs/1808.00206.

Hindawi
Journal of Control Science and Engineering
Volume 2020, Article ID 8954704, 17 pages
https://doi.org/10.1155/2020/8954704

Research Article

Stator Current-Based Model Reference Adaptive Control for Sensorless Speed Control of the Induction Motor

Workagegn Tatek Asfu

Depertment of Electrical and Computer Engineering, Debre Berehan University, Debre Berhan, Ethiopia

Correspondence should be addressed to Workagegn Tatek Asfu; workagegntatek@gmail.com

Received 17 February 2020; Revised 15 September 2020; Accepted 25 September 2020; Published 15 October 2020

Academic Editor: Hassan Haes Alhelou

This paper described that the stator current-based model reference adaptive system (MRAS) speed estimator is used for the induction motor (IM) indirect vector speed control without a mechanical speed sensor. Due to high sensitivity of motor parameters variation at low speed including zero, stability analysis of MRAS design is performed to correct any mismatch parameters value in the MRAS performed to estimate the motor speed at these values. As a result, the IM sensorless control can operate over a wide range including zero speed. The performance of the stator current-based MRAS speed estimator was analyzed in terms of speed tracking capability, torque response quickness, low speed behavior, step response of drive with speed reversal, sensitivity to motor parameter uncertainty, and speed tracking ability in the regenerative mode. The system gives a good performance at no-load and loaded conditions with parameter variation. The stator current-based MRAS estimator sensorless speed control technique can make the hardware simple and improve the reliability of the motor without introducing a feedback sensor, and it becomes more important in the modern AC IM. The sensorless vector control operation has been verified by simulation on Matlab and experimentally using Texas Instruments HVMTRPFCKIT with TMS320 F28035 DSP card and 0.18 kw AC IM.

1. Introduction

Induction motors chosen for variable speed drives due to primarily low material and manufacturing cost and also reliable, associated with the squirrel cage induction motor, are proposed by [1, 2]. As a result, induction motors are typically used in low and medium cost drive applications, which required moderate performance, such as conveyor belts, fans, and pumps. In [3–5], the authors proposed that accurate speed identification is required for all high-performance vectors that controlled IM drives. The speed identification of the IM can be performed by a shaft speed encoder. However, compared to speed estimation, a shaft speed encoder has several disadvantages such as an increase in cost, size, complexity, and maintenance requirements and a decrease in the reliability and robustness.

Shaft speed encoders are expensive and introduce reliability concerns for vector-controlled AC motor drives. The use of this encoder implies additional electronics, extra wiring, space, and careful mounting, which detracts from the inherent robustness of cage induction motors been proposed in [6]. Therefore, it has been a great interest in the research community in developing a high-performance induction motor drive that does not require a speed or position encoder for its operation. Different literatures proposed that the rotor speed of the induction motor has been estimated by various techniques. In [7], the rotor speed was estimated using angular velocity and slip calculation, the researchers used stator current and voltage as the reference model, and the performance of the system at operating (rated) speed was robust and simple to implement. However, the accuracy is not very good due to the great sensitivity to motor parameter variation. In [8], the state estimator for the induction motor was based on the extended Kalman filter. The estimation of rotor speed is by using nonlinear state estimation and is more robust to the IM parameter changes or identification errors but much more complicated in practical realization. The method required complexity mathematical analysis, and

the system needs high speed computation memory. The solution for rotor speed estimation is based on stator current-based MRAS principle, in which an error vector is formed from the outputs of reference and adaptive models, models both dependent on different motor parameters. The error is driven to zero through adjustment of the parameter that influences one of the models. The MRAS approach has advantages such as simplicity and easy to implement and has direct physical interpretation. So, stator current-based MRAS solves the problem due to aging, unmodel dynamics, and parameter variation even at low speed.

The stator current-based MRAS speed estimator has been designed and test through various software tools. In this paper, design and implementation of an adaptive estimator using the Matlab simulation and implementation using Texas Instruments TMS320F28035 control card on the general purpose AC induction motor was performed.

2. Indirect Field-Oriented Control

In the indirect field-oriented control (IFOC), the rotor flux angle is being measured indirectly, instead of using air gap flux sensors. IFOC estimates the rotor flux by computing the slip speed. The stationary d and q axes are fixed on the stator, and the rotor d and q axes are fixed on the rotor flux. The synchronous d and q axes are rotating at a synchronous speed, and so, there is a slip difference between the rotor speed and the synchronous speed. In order to ensure decoupling between the rotor flux and the torque, the torque component of the current should be aligned with the synchronous q-axis, and the stator flux component of current should be aligned with the synchronous d-axis.

In [9], the stator and rotor voltage equation of the induction motor in the field orientation synchronous reference frame was described. The general block diagram of the stator current-based MRAS speed estimator is shown in Figure 1.

3. Model Reference Adaptive System Design

Speed estimation methods using MRAS can be classified into various types according to the state variables. The most commonly used are the rotor flux-based MRAS, reactive power MRAS, back emf-based MRAS, and stator current-based MRAS. In [10, 11], in the rotor flux-based MRAS, the rotor flux is used as an output value for the model to estimate the rotor speed. In rotor flux-based MRAS, the presence of an open integration in the stator leads to problems with initial conditions and drift. A low-pass filter may be used instead of the pure integration; however, it has a degrading effect on speed estimation at low speeds and introduces time delay. The model reference adaptive approach based on back emf rather than the rotor flux offers an alternative to avoid the problem of pure integration. The pure integration is avoided in this approach, and there are no low-pass filters that create a bandwidth limit. A more severe source of inaccuracy is a possible mismatch of the reference model parameters and particularly of the stator resistance proposed by Rashed and Stronach in [12]. The solution for these problems is using the stator current-based MRAS speed estimator based on the comparison between the measured stator current of the IM and the estimated current obtained from the stator current model, which is used to estimate the rotor speed.

As shown in Figure 2, the stator current-based MRAS speed estimation structure consists basically of a reference model, adjustable model, and an adaptive mechanism. The reference model, which is independent of the rotor speed, calculates the state variable $(i_{s\alpha}, i_{s\beta})$ from the induction motor model and the adjustable model, which is dependent on the rotor speed, and estimates the state variables $(\hat{i}_{s\alpha}, \hat{i}_{s\beta})$ and $(\hat{\varphi}_{r\alpha}, \hat{\varphi}_{r\beta})$. The error between measured and estimated state variables is then used to drive an adaptation mechanism, which generates the estimated speed, for the adjustable model as shown in the block diagram of Figure 2.

3.1. Stator Current-Based MRAS Speed Estimator Design. The stator current-based MRAS speed estimator design is based on the comparison between the measured stator current of the IM and the estimated current obtained from the flux current model as shown in Figure 3. Using stator and rotor voltage and current equation, the mathematical model of the rotor flux and the stator current are estimated in stationary reference frames as follows.

$$\frac{\mathrm{d}\hat{i}_{s\beta}}{\mathrm{d}t} = \frac{1}{\sigma L_s}\left(v_{s\beta} - R_s\hat{i}_{s\beta} - \frac{L_m^2}{L_r T_r}\hat{i}_{s\beta} + \frac{L_m}{L_r T_r}\hat{\varphi}_{r\beta} + \frac{L_m}{L_r}\,\hat{\omega}_r\hat{\varphi}_{r\alpha}\right), \tag{1}$$

$$\frac{\mathrm{d}\hat{i}_{s\alpha}}{\mathrm{d}t} = \frac{1}{\sigma L_s}\left(v_{s\alpha} - R_s\hat{i}_{s\alpha} - \frac{L_m^2}{L_r T_r}\hat{i}_{s\alpha} + \frac{L_m}{L_r T_r}\hat{\varphi}_{r\alpha} + \frac{L_m}{L_r}\,\hat{\omega}_r\hat{\varphi}_{r\beta}\right), \tag{2}$$

$$\frac{\mathrm{d}}{\mathrm{d}t}\hat{\varphi}_{r\beta} = \frac{L_m}{L_r}\,\hat{i}_{s\beta} - \frac{1}{T_r}\hat{\varphi}_{r\beta} + \hat{\omega}_r\hat{\varphi}_{r\alpha}, \tag{3}$$

$$\frac{\mathrm{d}}{\mathrm{d}t}\hat{\varphi}_{r\alpha} = \frac{L_m}{L_r}\,\hat{i}_{s\alpha} - \frac{1}{T_r}\hat{\varphi}_{r\alpha} - \hat{\omega}_r\hat{\varphi}_{r\beta}. \tag{4}$$

In the stator current-based MRAS rotor speed estimator, the adaptation algorithm is based on the error between estimated and measured stator current based on the Lyapunov function. The adaptation mechanism can be derived from the adaptive stator current, and rotor flux estimator is constructed as follows. Considering the Lyapunov function candidate [13], rearrange equations (1)–(4) in the matrix form:

Let, $\dot{x} = Ax + B\overrightarrow{v_s}$ and $y = Cx$, where system matrix A is written as follows

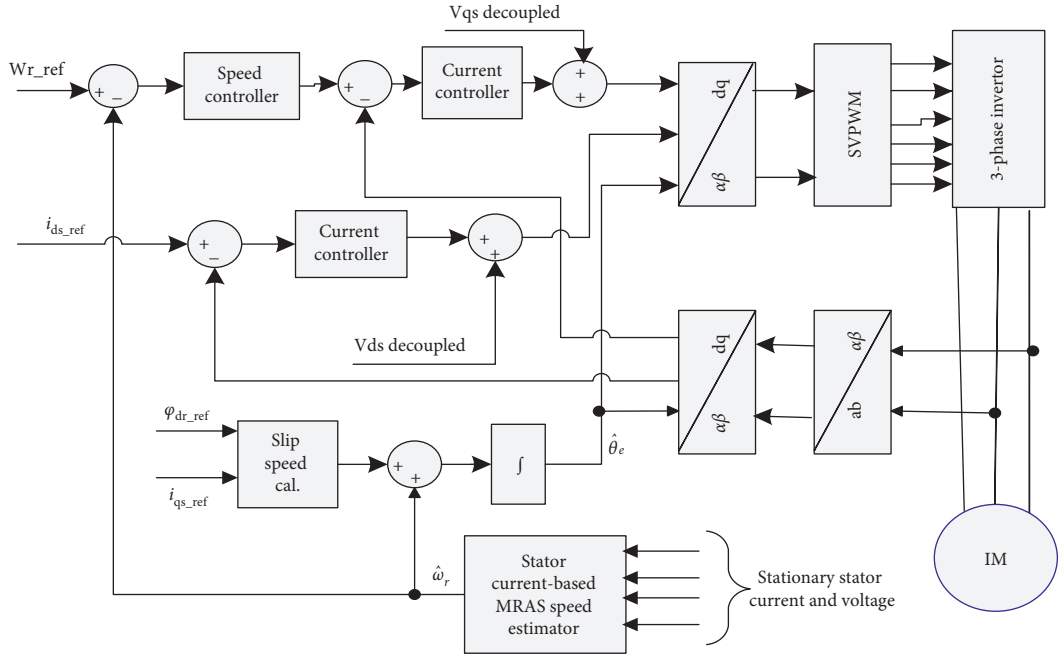

Figure 1: General block diagram of MRAS-based sensorless speed control of the induction motor.

$$A = \begin{bmatrix} \frac{-1}{\sigma L_s}\left(R_s + \frac{L_m^2}{L_r T_r}\right) & 0 & \frac{1}{\sigma L_s}\frac{L_m}{L_r T_r} & \frac{1}{\sigma L_s}\frac{L_m}{L_r}\widehat{\omega}_r \\ 0 & \frac{-1}{\sigma L_s}\left(R_s + \frac{L_m^2}{L_r T_r}\right) & \frac{-1}{\sigma L_s}\frac{L_m}{L_r}\widehat{\omega}_r & \frac{1}{\sigma L_s}\frac{L_m}{L_r T_r} \\ \frac{L_m}{T_r} & 0 & \frac{-1}{T_r} & \widehat{\omega}_r \\ 0 & \frac{L_m}{T_r} & \widehat{\omega}_r & \frac{-1}{T_r} \end{bmatrix},$$

$$B = \frac{-1}{\sigma L_s}.C^T,$$

$$C = \begin{bmatrix} 1 & 0 & 0 & 0 \\ 0 & 1 & 0 & 0 \end{bmatrix},$$

$$\frac{\mathrm{d}v}{\mathrm{d}t} = \left\{\varepsilon^T\left[A^T + A\right]\varepsilon - 2\left(\omega_r - \widehat{\omega}_r\right)\left[k\left(\varepsilon_{i\alpha}\widehat{\varphi}_{r\beta} - \varepsilon_{i\beta}\widehat{\varphi}_{r\alpha}\right) - \frac{1}{\gamma}\frac{\mathrm{d}}{\mathrm{d}t}\widehat{\omega}_r\right]\right\}, \tag{5}$$

$$\varepsilon^T\left[A^T + A\right]\varepsilon < -Q, \tag{6}$$

$$y = C\widehat{x}. \tag{7}$$

Let $\varepsilon_{i\alpha} = i_{\alpha s} - \widehat{i}_{\alpha s}$, and $\varepsilon_s = i_s - \widehat{i}_s$, where $i_s = \begin{bmatrix} i_{\alpha s} \\ i_{\beta s} \end{bmatrix}$, $\varepsilon_{i\beta} = i_{\beta s} - \widehat{i}_{\beta s}$, and $\varepsilon_\omega = \omega_r - \widehat{\omega}_r$.

$v = v_1 + v_2$. Let $v_1 = \varepsilon^T\varepsilon$ and $v_2 = \varepsilon_\omega^2/\gamma$, and the derivative of this Lyapunov candidate function written as $x - \widehat{x}$.

The derivative of this Lyapunov candidate function written as $\mathrm{Q} = \rho I_n$ and $\rho > 0$, and it is an identity matrix.

Using the Lyapunov stability of the adaptive estimator has been proved if two conditions are fulfilled. The eigenvalues of the estimator are selected to have negative real parts, so that the states of the estimator will converge to the desired states of the estimated system. The term in factor of $(\omega_r - \widehat{\omega}_r)$ in equation (5) must be zero. The expression of the derivative of estimated speed becomes

$$k\left(\varepsilon_{i\alpha}\widehat{i}_{s\beta} - \varepsilon_{i\beta}\widehat{\varphi}_{r\alpha}\right) - \frac{1}{\gamma}\frac{\mathrm{d}}{\mathrm{d}t}\widehat{\omega}_r = 0,$$

$$\frac{\mathrm{d}}{\mathrm{d}t}\widehat{\omega}_r = \gamma k\left(\varepsilon_{i\alpha}\widehat{\varphi}_{r\beta} - \varepsilon_{i\beta}\widehat{\varphi}_{r\alpha}\right),$$

$$\widehat{\omega}_r = M\int\left(\varepsilon_{i\alpha}\widehat{\varphi}_{r\beta} - \varepsilon_{i\beta}\widehat{\varphi}_{r\alpha}\right)\mathrm{d}t. \tag{8}$$

However, this adaptive law of the speed has been obtained by adjusted M (finite positive constant). For improving the dynamic of this estimator during the transitory phase of the rotor speed, estimate the speed by a large PI regulator; so, it requires a supplementary term proportional. Then,

$$\widehat{\omega}_r = \mathrm{ki}\int\left(\varepsilon_{i\alpha}\widehat{\varphi}_{r\beta} - \varepsilon_{i\beta}\widehat{\varphi}_{r\alpha}\right)\mathrm{d}t + \mathrm{kp}\left(\varepsilon_{i\alpha}\widehat{\varphi}_{r\beta} - \varepsilon_{i\beta}\widehat{\varphi}_{r\alpha}\right), \tag{9}$$

where k_i and k_p are the adaptive gains for the speed estimator.

3.2. Stability Analysis of the Stator Current-Based MRAS Speed Estimator. The stability analysis of the stator current-based MRAS speed estimator is tested from the point of the IM and

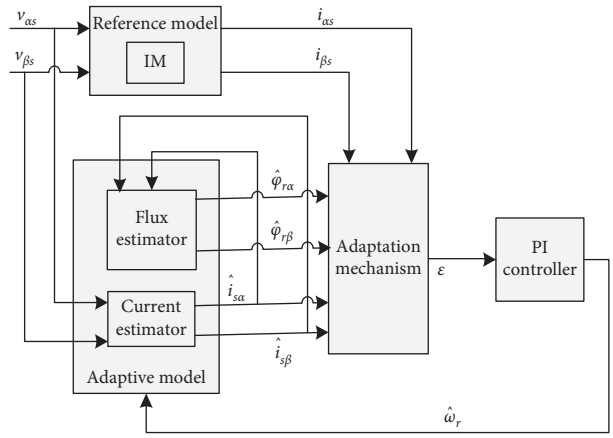

Figure 2: General block diagram of the stator current-based MRAS speed estimator.

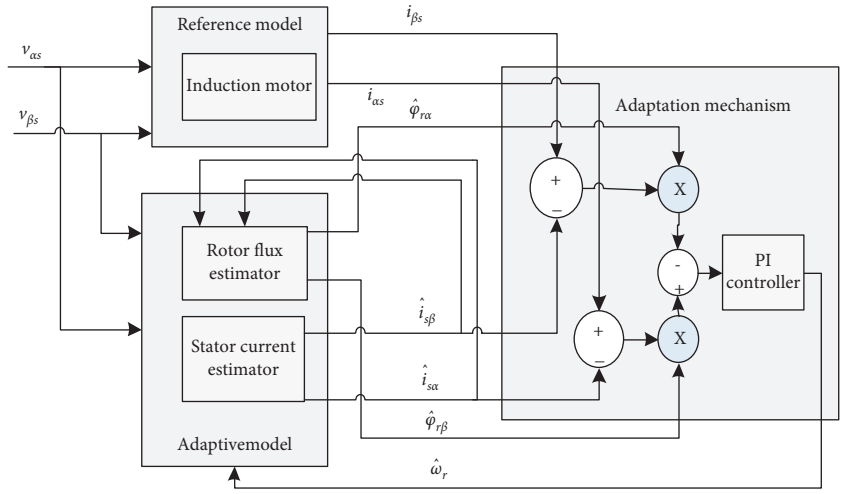

Figure 3: Adaptation mechanisms for the stator current-based MRAS speed estimator.

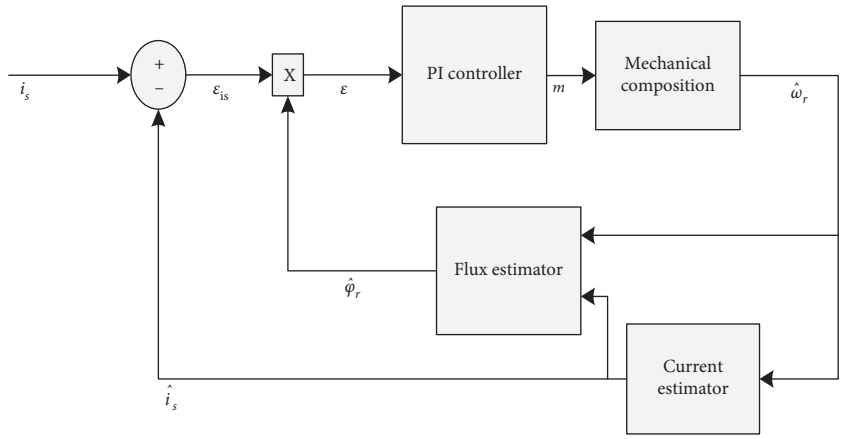

Figure 4: Closed loop stator current-based MRAS speed estimator with mechanical compensation.

PI controller parameter changes, on the basis of the estimator transfer function. From the point of view of the rotor speed estimation, the stator current-based MRAS speed estimator can be analyzed as a system controlled by the signal, which is the combination of the stator current and the rotor flux used in the adaptation loop. To find the value of

the PI adaptive gains, analyze the closed loop transfer function of the stator current-based MRAS speed estimator (Figure 4).

The mechanical model of the system at stationary reference frame is obtained as follows.

$$\frac{\mathrm{d}}{\mathrm{d}t}\widehat{\omega}_r = \frac{3\mathrm{pL}_m}{4\mathrm{JL}_r}\left(\varphi_{\alpha r} i_{\beta s} - \varphi_{\beta r} i_{\alpha s}\right) - \frac{f}{J}\omega_r - \frac{\mathrm{Tl}}{J}. \tag{10}$$

In order to drive the PI controller parameter, a linearized transfer function between $m_{(s)}$ and $\varepsilon_{(s)}$ is obtained. Using small signal analysis under the assumption of field orientation, the difference between the measured and the estimated value, with the operating point, is written as

$$\begin{aligned} \Delta y &= C\Delta x = C\,(\mathrm{SI} - A)^{-1}\Delta A x_0, \\ \Delta \dot{x} &= A\Delta x + \Delta A x_0, \end{aligned} \tag{11}$$

where $\Delta x = (x - \hat{x})$, and $x_0 = [i_{\mathrm{ds0}}\, i_{\mathrm{qs0}}\, \varphi_{\mathrm{dr0}}\, \varphi_{\mathrm{qr0}}]^T$.

The system matrix A is expressed as follows, considering the rotor speed as the only variable parameter.

$$\begin{aligned} \Delta A &= \begin{bmatrix} 0 & 0 & 0 & a \\ 0 & 0 & -a & 0 \\ 0 & 0 & 0 & -1 \\ 0 & 0 & 1 & 0 \end{bmatrix} \Delta\omega_r, \\ \text{where, } a &= \frac{1}{\sigma L_s}\frac{L_m}{L_r}, \\ \Delta y &= \begin{bmatrix} i_{\alpha s} - \widehat{i}_{\alpha s} \\ i_{\beta s} - \widehat{i}_{\beta s} \end{bmatrix} \\ \mathrm{adj}\,(\mathrm{SI} - A) &= \begin{bmatrix} a_{11} & a_{12} & a_{13} & a_{14} \\ a_{12} & a_{22} & a_{23} & a_{24} \\ a_{31} & a_{32} & a_{33} & a_{34} \\ a_{41} & a_{42} & a_{43} & a_{44} \end{bmatrix}, \end{aligned} \tag{12}$$

$$\begin{bmatrix} \dfrac{\Delta i_{\alpha s}}{\Delta \omega_r} \\ \dfrac{\Delta i_{\beta s}}{\Delta \omega_r} \end{bmatrix} = C\,(\mathrm{SI} - A)^{-1} \begin{bmatrix} 0 & 0 & 0 & a \\ 0 & 0 & -a & 0 \\ 0 & 0 & 0 & -1 \\ 0 & 0 & 1 & 0 \end{bmatrix} \left[i_{\mathrm{ds0}}\, i_{\mathrm{qs0}}\, \varphi_{\mathrm{dr0}}\, \varphi_{\mathrm{qr0}}\right]^T. \tag{13}$$

Then, substitute equation (12) into equation (13), and solving Δw_r from the mechanical model, the transfer function of $m_{(s)}$ and $\varepsilon_{(s)}$ is obtained.

From equation (12) and the adjoint of $(\mathrm{SI} - A)$,

$$\varepsilon = -\frac{(a_{24} - a\,a_{22})}{|\mathrm{SI} - A|}\,\widehat{\varphi}_{\alpha r0}^2 \Delta\omega_r. \tag{14}$$

Then, the transfer function between $\varepsilon_{(s)}$ and $m_{(s)}$ is obtained as

$$\frac{\varepsilon(s)}{m(s)} = \left\{ -\frac{(a_{24} - a\,a_{22})}{|\mathrm{SI} - A|}\,\frac{1}{(s + (f/J))}\,\frac{p}{2J}\widehat{\varphi}_{\alpha r0}^2 \right\}. \tag{15}$$

Let $G(s)$ and $\varepsilon(s)/m(s)$ are then the simplified closed loop block diagram of the stator current-based MRAS speed estimator as shown in Figure 5.

$$\frac{\omega_r}{\widehat{\omega}_r} = \left\{ \frac{\left(G_{(s)}\left(\mathrm{kp}_{\mathrm{mras}} + \left(\mathrm{ki}_{\mathrm{mras}}/s\right)\right)\right)}{1 + \left(G_{(s)}\left(\mathrm{kp}_{\mathrm{mras}} + \left(\mathrm{ki}_{\mathrm{mras}}/s\right)\right)\right)} \right\}. \tag{16}$$

The design of k_p and k_i is introduced to ensure stability, error tracking, and robust operation. The design criteria for this adaptive PI controller are performed using Matlab/SISOTOOL, by using the transfer function of the plant and set the time domain constraint. The constraint considered in this design is that the percentage of overshoot, settling time, and rise time are less than five percentage, less than two second, and less than two second, respectively.

As shown in Figure 6, the design is selected to ensure that all the poles and zeros are located in the left hand side of the s-plane, and this allows for the required fast and stable response.

4. Simulation Results and Discussion

The proposed control system represented in Figure 1 is designed for simulation by the Matlab/Simulink model. Simulation results are presented and discussed to show the effectiveness of the proposed drive system based on the stator current-based MRAS speed estimator and IFOC at different operating conditions. For studying the performances of proposed system, a series of simulations and measurements have been carried out. In this respect, the dynamic response of the proposed speed estimation algorithm is studied under different speed commands.

4.1. Simulation Results. The simulation result of MRAS-based sensorless speed control of the induction motor drive was carried out to assess its performance. Knowledge of motor's parameter is important for this simulation, since the estimator is highly parameter dependent, and the effect of the parameter variation was tested based on different conditions that are put on their effects on robustness of the speed control.

The first simulation result for the MRAS-based sensorless speed control of the induction motor is the three-phase stator current, which is generated by the three-phase voltage source inverter. This three phase voltage source inverter is controlled by SVPWM blocks for appropriate stator current generation. These three phases of current should be of equal magnitude and 120° phase shift with each other for appropriate rotating flux generation as shown in Figure 7.

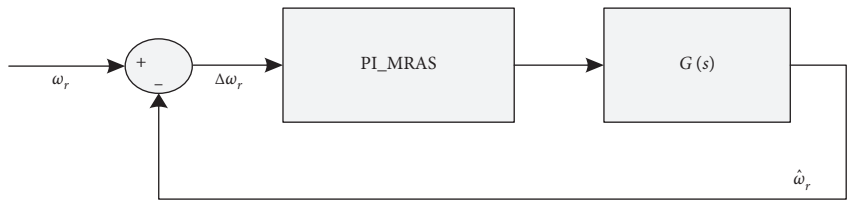

Figure 5: Closed loop block diagram of the stator current-based MRAS speed estimator.

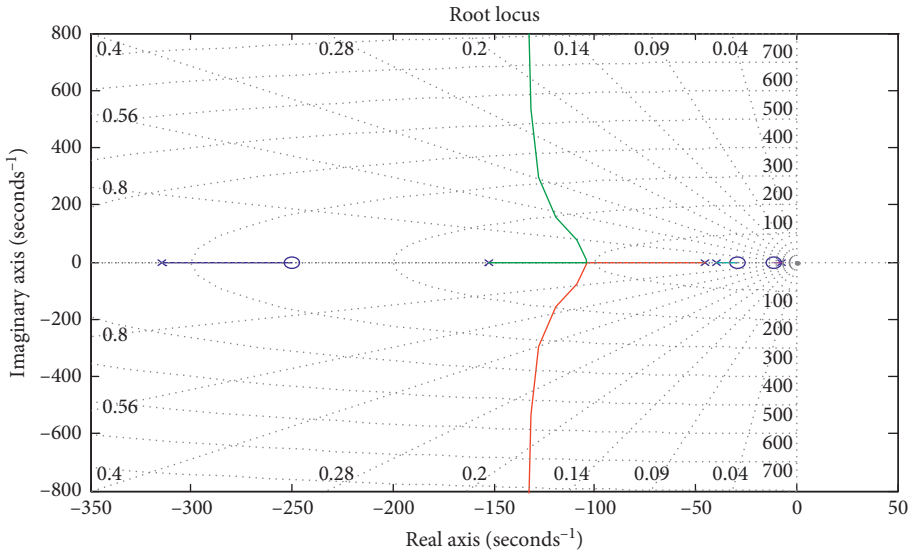

Figure 6: Root locus of the closed loop adaptive control system.

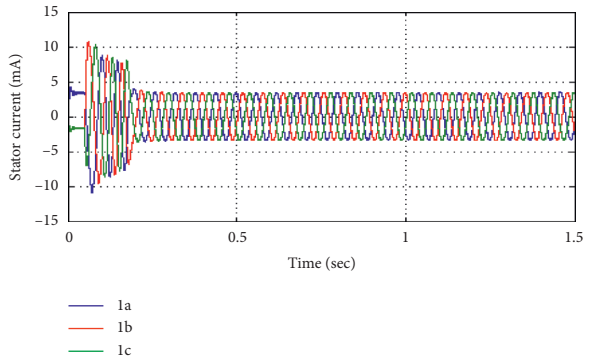

Figure 7: Three-phase stator current at 100 rad/s.

As it has been seen from the Figure 7, the appropriate stator phase current is generated with good accuracy. Hence, the system can feed the appropriate stator voltage to the motor. If the voltage applied to the motor is applied with appropriate magnitude and frequency, the speed of the motor is respected as a set to the reference value.

The simulation results of the proposed stator current-based MRAS speed estimator for sensorless speed control of the induction motor drive is discussed in terms of set point tracking capability, torque response quickness, low speed behavior, step response of drive with speed reversal, sensitivity to motor parameter uncertainty, and speed tracking ability in the regenerative mode.

4.1.1. Set Point Tracking Capability. It is always crucial to know the performance of an estimator based on the ability of the estimated speed to converge the actual value, especially during the transient response. This criterion has been well accepted as a primary indicator when benchmarking the performance of a sensorless speed estimator. Using the same parameters in the induction motor and the stator current-based MRAS speed estimator, the tracking performance of the estimator can be examined by changing the speed reference of the system. As shown in Figures 8(a) and 8(c), the proposed estimator tracks both the step and square signals reference input. This shows the tracking performance of the estimator, and the actual speed to the reference speed can be examined by changing the reference of the system with the maximum steady state error of 0.0027% and good transient performance with rise time less than 0.1 second. As shown in Figure 8(b), the estimated angle follows with the actual angle with the maximum error of 0.1 rad. Figure 9(a) shows the variable speed driving of the induction motor with step speed response, the actual, and the estimated speed track the reference speed at every 0.13 seconds. As shown in Figure 9(b), the actual speed and the estimated speed follow the reference with variable step input for 0.75 seconds and the input change to sine to check its tracking capability for different inputs. From this result, the proposed system operates for different

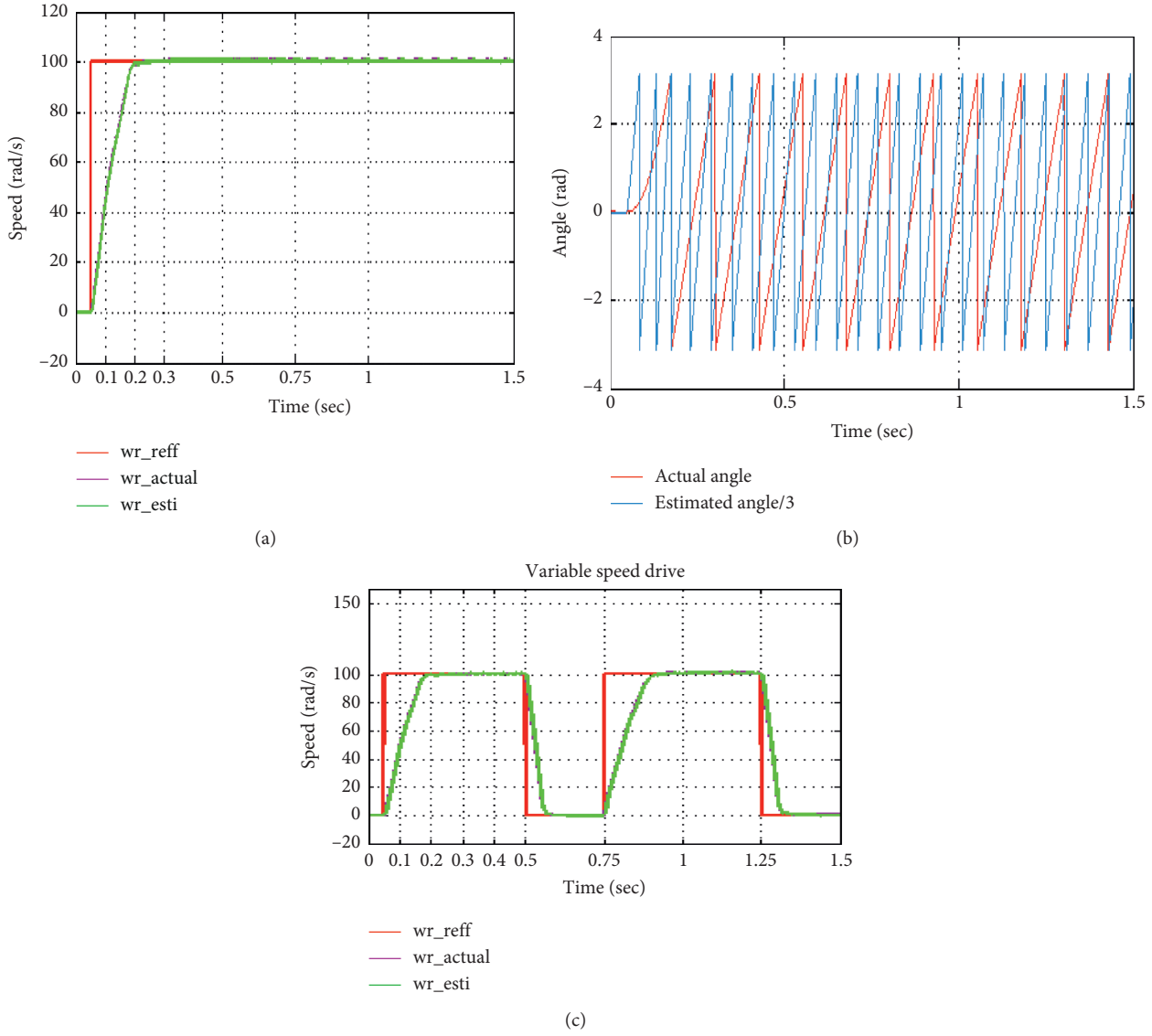

Figure 8: Speed response for square and step reference speed in rad/s and the estimated angle.

inputs with a good accuracy of steady state and transient responses.

4.1.2. Torque Response Quickness. To find the torque response quickness, the motor is started with 1 Nm load torque, and this value is increased to 2 Nm, and after 0.2 second, this results in a drop in the motor speed. This happens because of the mismatch in the torques, i.e., the developed torque is less than the load torque. To compensate for this mismatch, the controller increases the developed torque; then, the motor speed increases and comes back to the set point as shown in Figure 10.

4.1.3. Low and Zero Speed Behavior. The aim of this test is to evaluate the performance of the stator current-based MRAS speed estimator at low speed. Figure 11(a) shows that the estimated speed follows the actual speed exactly, the reference speed is very close with the steady state error of 0.024 rad/s, and a good transient performance rise time less than 0.1 second. There is also good field orientation down to zero speed as shown in Figure 11(b). This means that the system is stable at zero spee $\widehat{\omega}_r$d, and continuous operation is possible. There is a short period, and the $\omega_{r-\text{act}}$ and settle to their respective steady state values.

4.1.4. Step Response of Drive with Speed Reversal. Figure 12 shows the simulation result for speed reversal in step input. The motor reference speed is changed from 75 rad/s to −35 rad/s at 0.5 seconds, and again, speed is set to 75 rad/s at 1 second. The result shows that the actual and estimated speed takes 0.09 second to follow the reference speed with good accuracy transient response. Reference speed and actual speeds are plotted in the same scale to observe the accuracy of the stator current-based MRAS speed estimator.

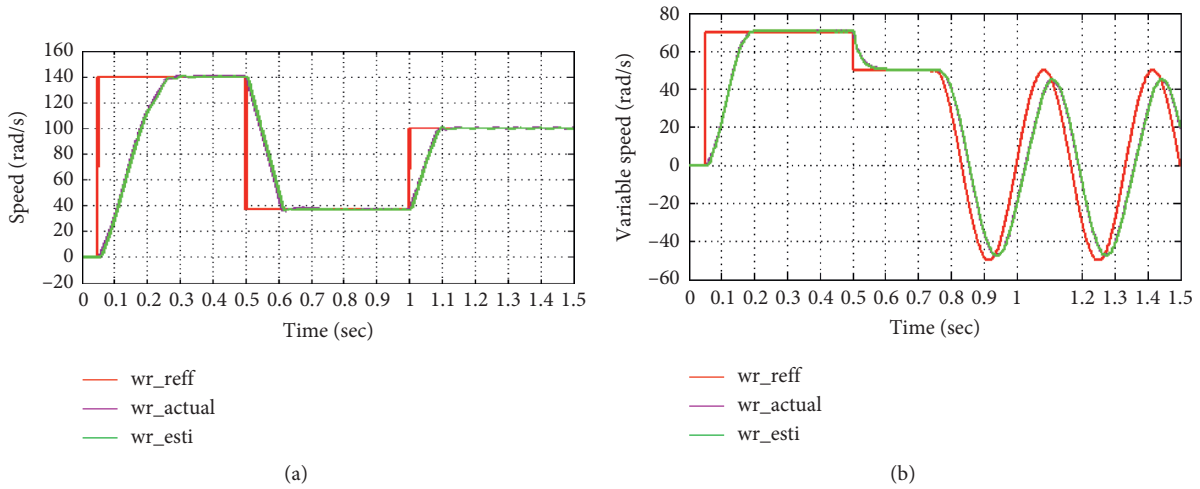

Figure 9: Variable speed step response in rad/s with a load torque of 2 Nm.

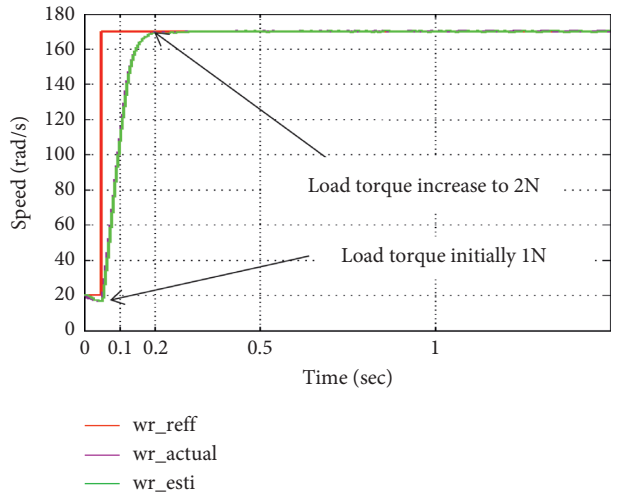

Figure 10: Load torque effect on stator current-based MRAS.

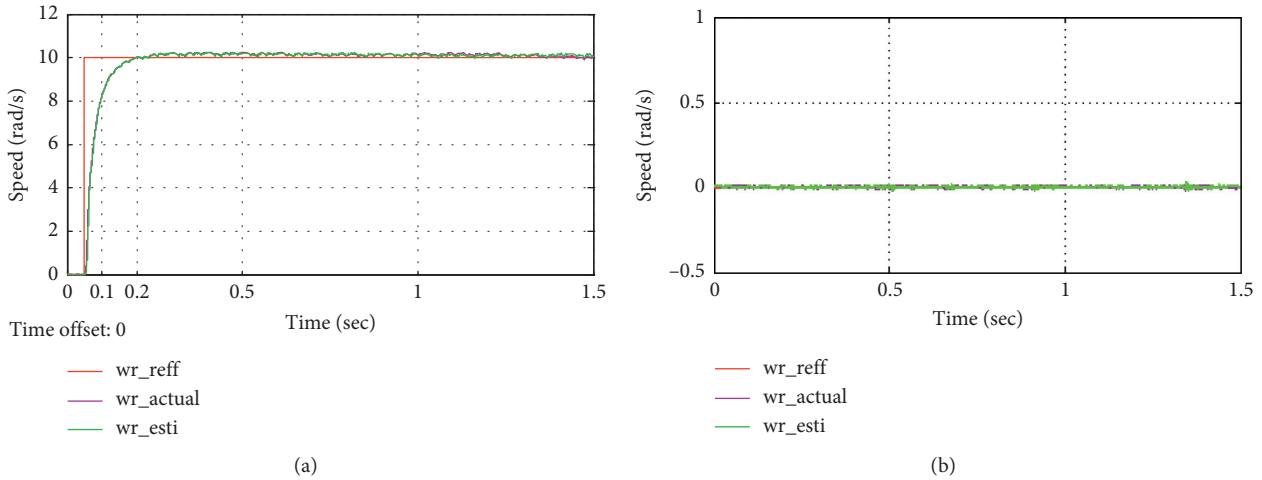

Figure 11: Step response for 10 rad/s and zero rad/s speed response with no load torque.

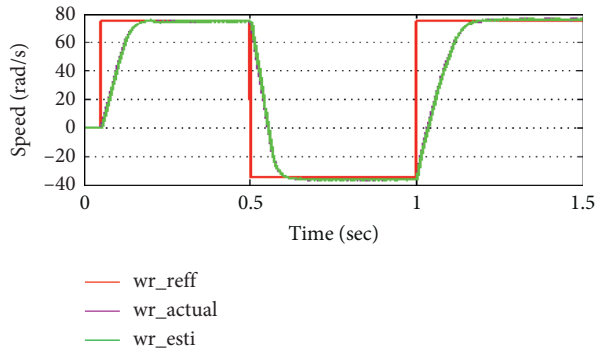

Figure 12: Step response of drive with speed reversal with load.

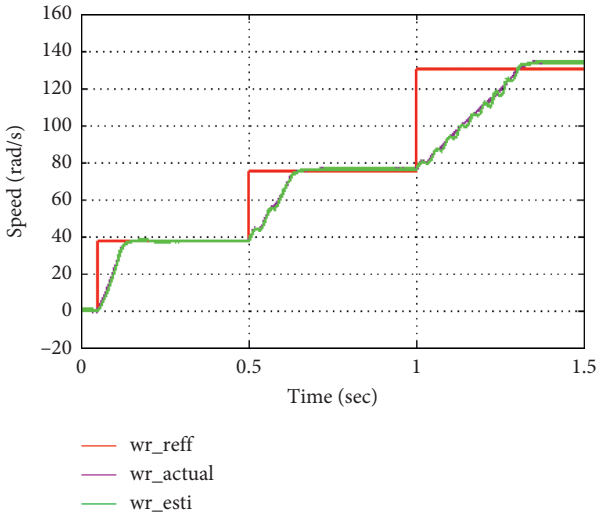

Figure 13: 75% increase of all parameters from their nominal value for different rotor speeds.

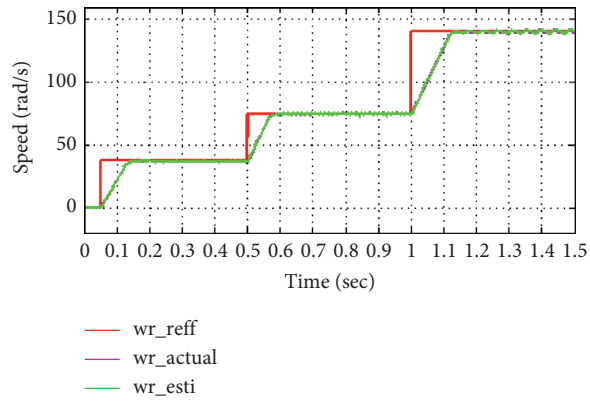

Figure 14: 75% decrease of all parameters from their nominal value for different rotor speeds with load torque.

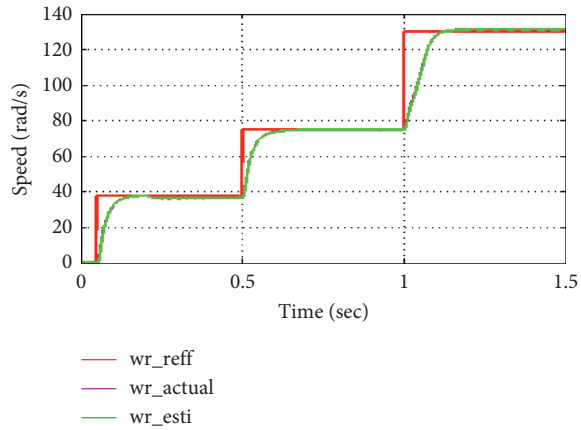

Figure 15: 50% decrease of R_s from its nominal value for different rotor speeds.

4.1.5. Parameter Sensitivity. The sensitivity to the motor parameters change has been tested for three reference speeds, namely, 100%, 50%, and 25% of the nominal speed; parameters R_s, L_s, R_r, and L_r have been changed by 75% from their nominal value. As shown in Figure 13, the sensitivity to motor parameter changes of the sensorless field oriented control with the stator current-based MRAS speed estimator is less sensitive to motor parameter variation. As shown in Figure 14, when the motor parameters decrease by 75% of their nominal value, the estimated speed exactly follows the actual speed and closely to the reference speed with a good accuracy of transient with rise time less 0.1 second with steady state error of less than 0.028 rad/s. In Figure 14, the speed estimator is much less sensitive to the IM parameter changes at low speed, and the sensitivity increases to some extent when the speed is near to its nominal speed, i.e., 140 rad/s.

The effect of stator and rotor resistance on the stator current-based MRAS speed estimator. Assume that the rotor and stator resistance vary by increasing 50% and decreasing 50% with their nominal value, and the other parameters are constant, with the speed 100%, 50%, and 25% of the rated value. As shown in Figures 15 and 16, when the stator resistance varies by 50% of its nominal value, the estimated speed exactly follows the actual speed and closely to the reference speed with a good accuracy of transient and steady state responses. As shown in Figures 17 and 18, when rotor resistance changes 50% from its nominal value, it has a good accuracy while the motor is running at low speed, while increasing the speed near to the nominal value, settling time and rise time increase compared to the lower speed. From this result, further increasing of the rotor resistance may affect the motor speed, while it runs near to its nominal speed.

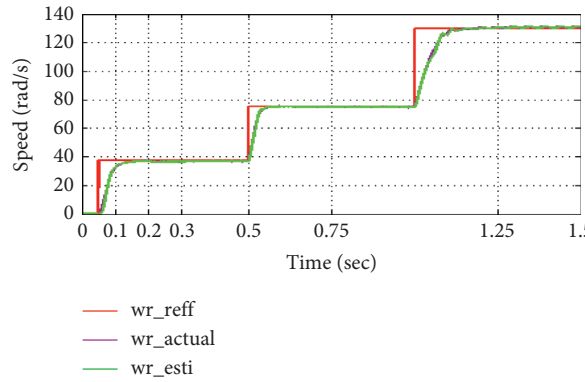

Figure 16: 50% increase of R_s from its nominal value for different rotor speeds.

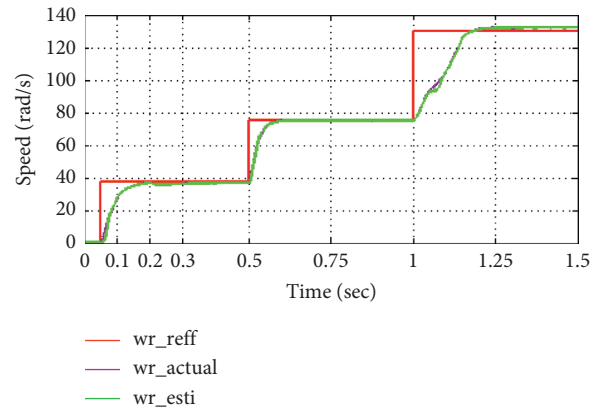

Figure 17: 50% decrease of R_r from its nominal value for different rotor speeds.

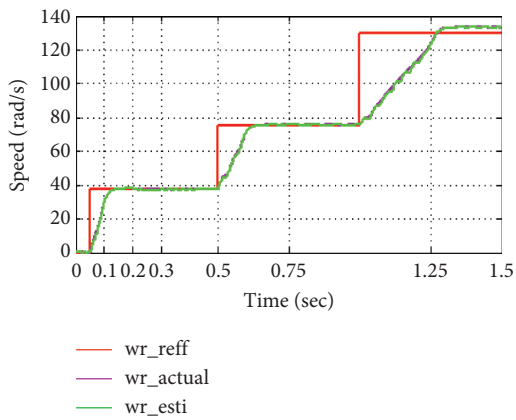

Figure 18: 50% increase of R_r from its nominal value for different rotor speeds.

4.1.6. Regenerative Mode. Motor speed is changed from +50 rad/s to −50 rad/s keeping the load torque constant at 2 Nm. The drive is operated in the motoring mode up to 1 second. Thereafter, it enters in the regenerating mode of operation for 0.5 seconds and comes back to motoring region after 0.5 seconds. As shown in Figure 19, the estimated and the actual speed follow the reference speed successfully.

From Figure 20, due to the increase of stator current in that region, i.e., for 0.05 second, starting of the motoring region, and at 0.5 second, the operation enters to the regenerating mode, and finally, it turns back to the motoring mode after one second. The stator current increases for transient response and turns to their rate value for the steady state response.

Staircase tracking waveform includes the low speed region: a reference speed of 5 rad/s was initially applied at $t = 0.05$ seconds, increased to 25 rad/s, 50 rad/s, and 100 rad/s at $t = 0.5$ seconds, $t = 0.75$ seconds, and at $t = 1$ second, respectively. As shown in Figure 21, the estimated and the actual speed follow the reference speed with good accuracy, and it takes 0.09 seconds to track the reference speed at different levels of speed including the low speed region.

5. Experimental Implementation

To test the performance of the proposed scheme, experiment is carried out on the IM with the same parameters simulation. Experimental setup of the induction motor control developed system is shown in Figure 22, which is based on a high voltage motor control developer's kit produced by Texas Instruments Company. The PWM frequency for the experiment is 60 kHz, and the ISR frequency of 10 kHz is selected for best operation of the motor. Experimental data

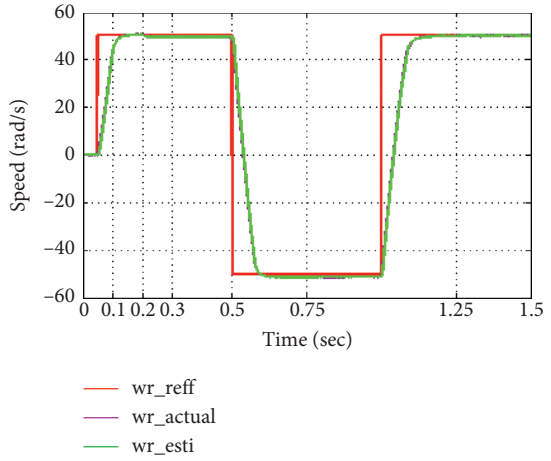

Figure 19: The actual and estimated speed performance in the regenerative mode.

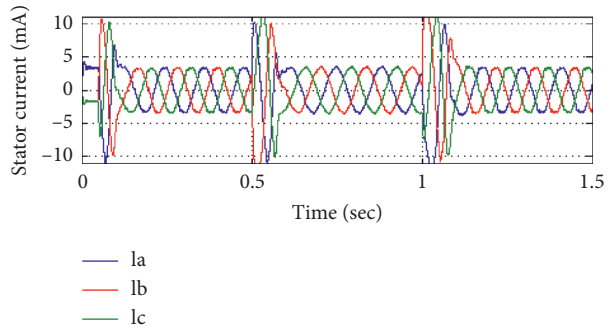

Figure 20: Stator current at motoring and regenerating modes.

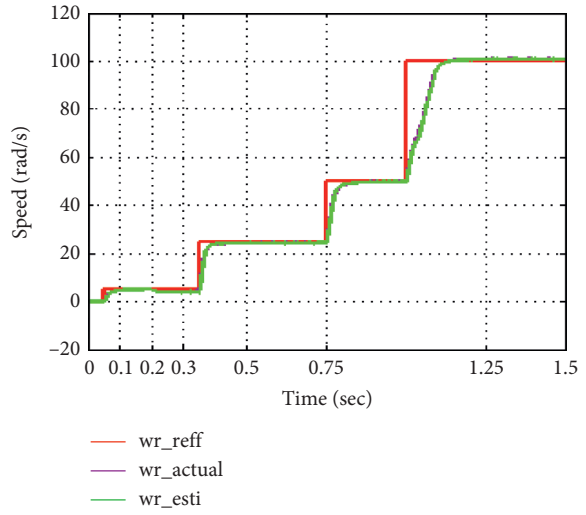

Figure 21: Speed response of staircase tracking waveform including the low speed region.

are captured for display and analysis via a graph tool in the Code Composer Studio (CCS).

The overall experimental system contains both hardware and software. The hardware includes the high voltage motor control kit with TMS320F28035 DSP control card, three-phase induction motor, PC with Code Composer Studio (CCS v6.0) installed, digital oscilloscope, digital multimeter, JTAG probe, rheostat, and high voltage DC power supply. The software includes different coordinate transformation algorithm, controller's algorithm, stator current-based MRAS speed estimator algorithm, space vector pulse width modulation algorithm, and the kit interrupt software algorithm. The overall experimental block diagram contains mainly three modules: Piccolo TMS320F28035 control card, high voltage motor control kit, and induction motor as shown in Figure 22.

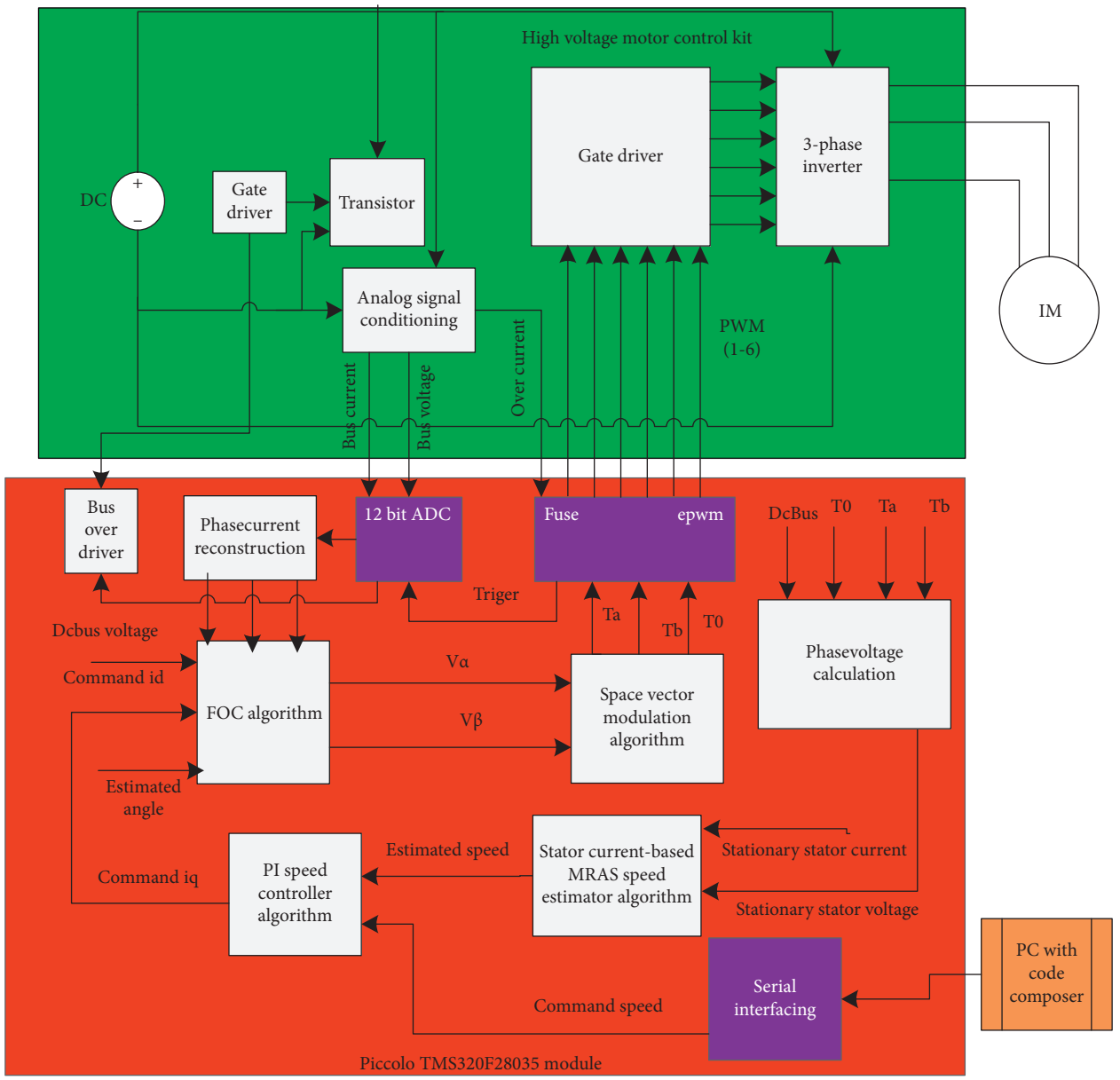

Figure 22: Experimental block diagram for MRAS-based sensorless speed control of the IM.

As shown in Figure 22, the high voltage motor control kit module includes gate driver, which controls the three-phase voltage source inverter, analog signal conditioning circuit used to sense stator current and DC bus voltage, and three-phase invertor to drive the motor. The second module is Piccolo TMS320F28035 control card consisting of control algorithms and hardware module. Control algorithms include the FOC, PI speed controller, phase current and voltage reconstruction, stator current-based MRAS speed estimator, and SVPWM algorithm. The hardware modules are indicated by purple color in Figure 22.

The digital motor control software library is the collection of digital motor control software modules. The library supports the AC IM and comprises both peripheral dependent software drives and TMS320F28035 control card dependent modules.

The overall system algorithm is based on two modules as shown in Figure 23. These are the initialization module and interrupt subroutine module.

5.1. Experimental Setup. The experimental setup of the MRAS-based sensorless speed control of an induction motor is shown in Figure 24. The experimental setup includes the

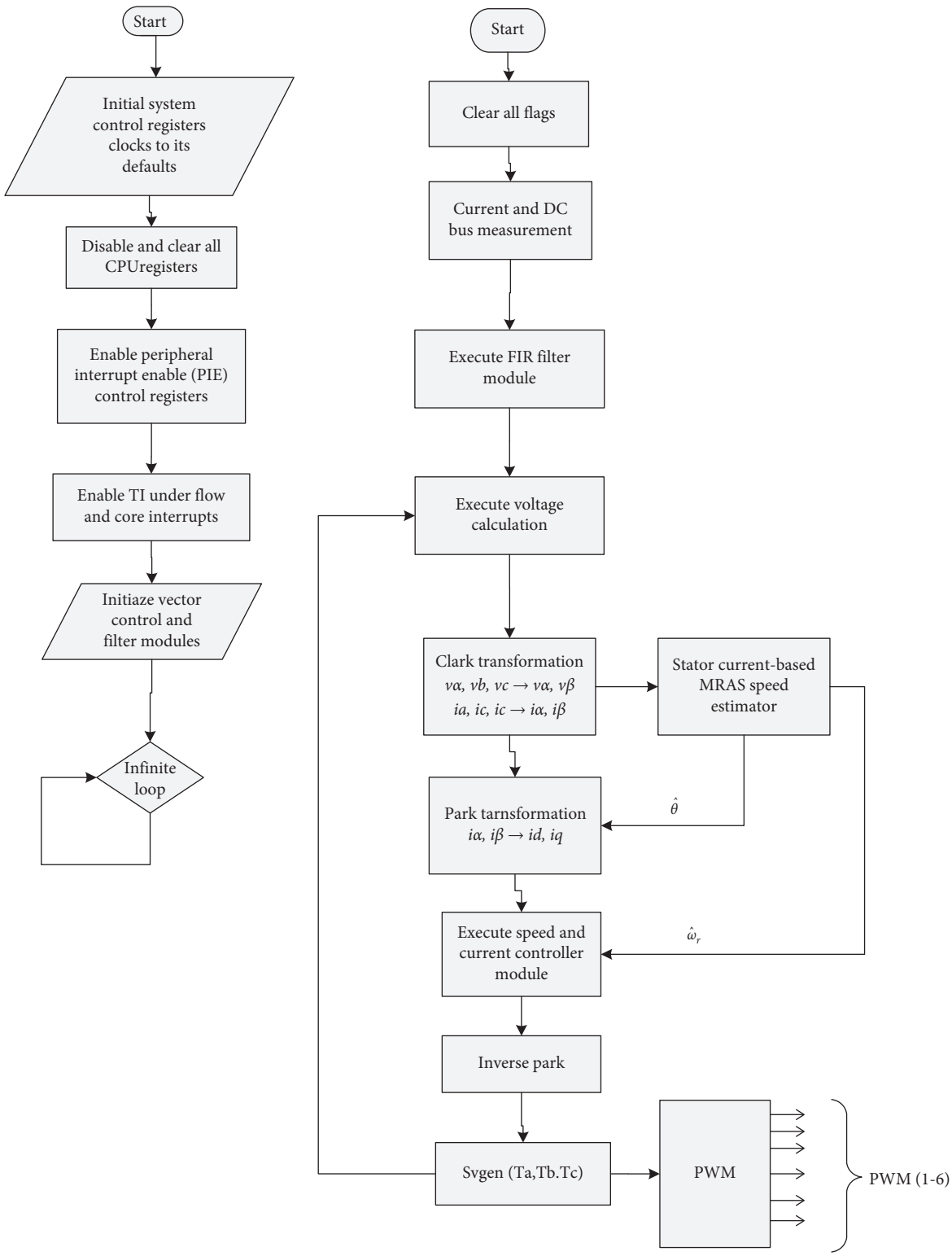

Figure 23: Flowchart of the proposed system.

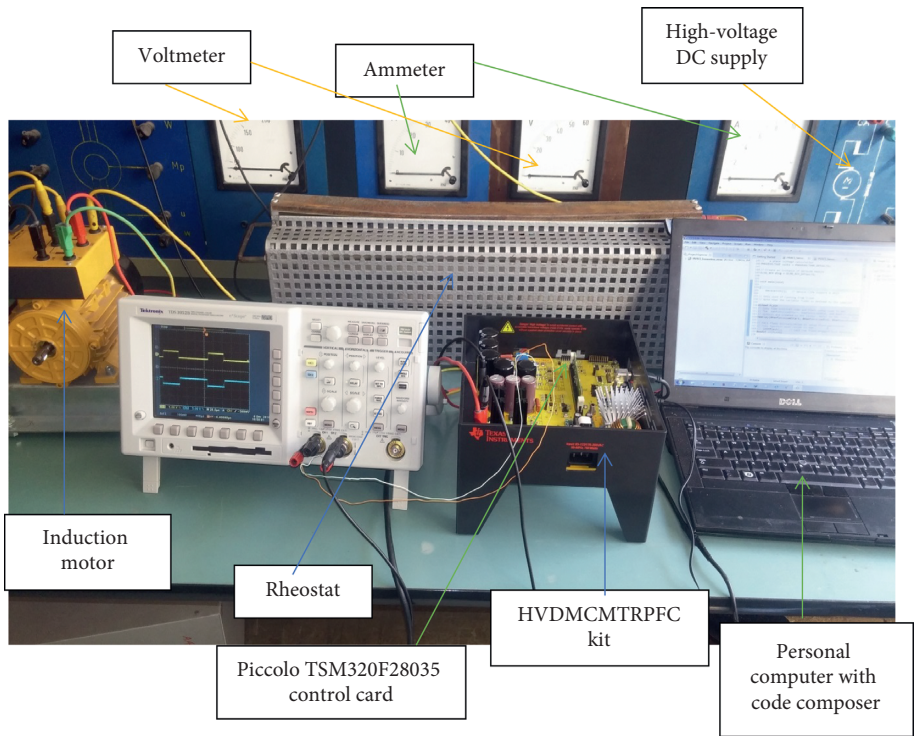

Figure 24: Experimental setup of the proposed system.

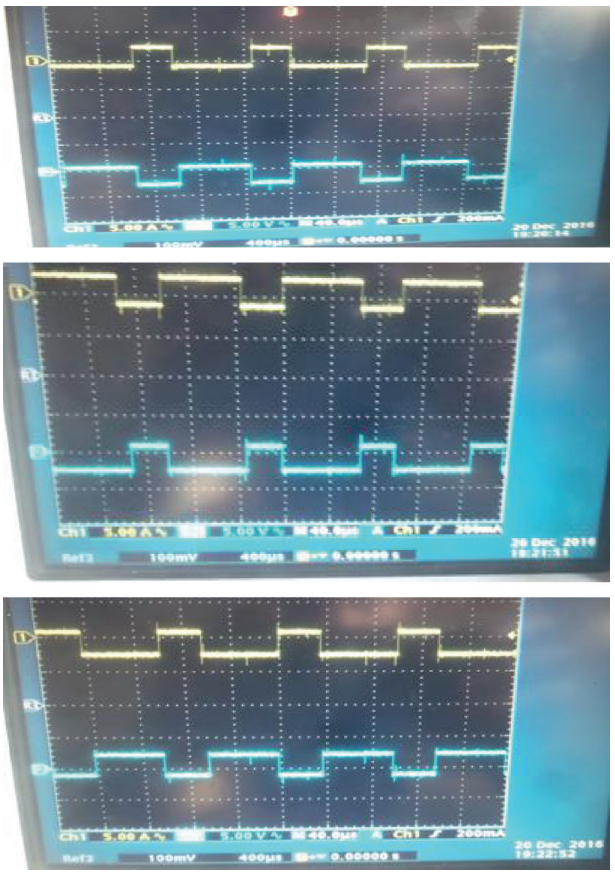

Figure 25: The six PWM output signals from DSP while the motor is running at 0.2 pu.

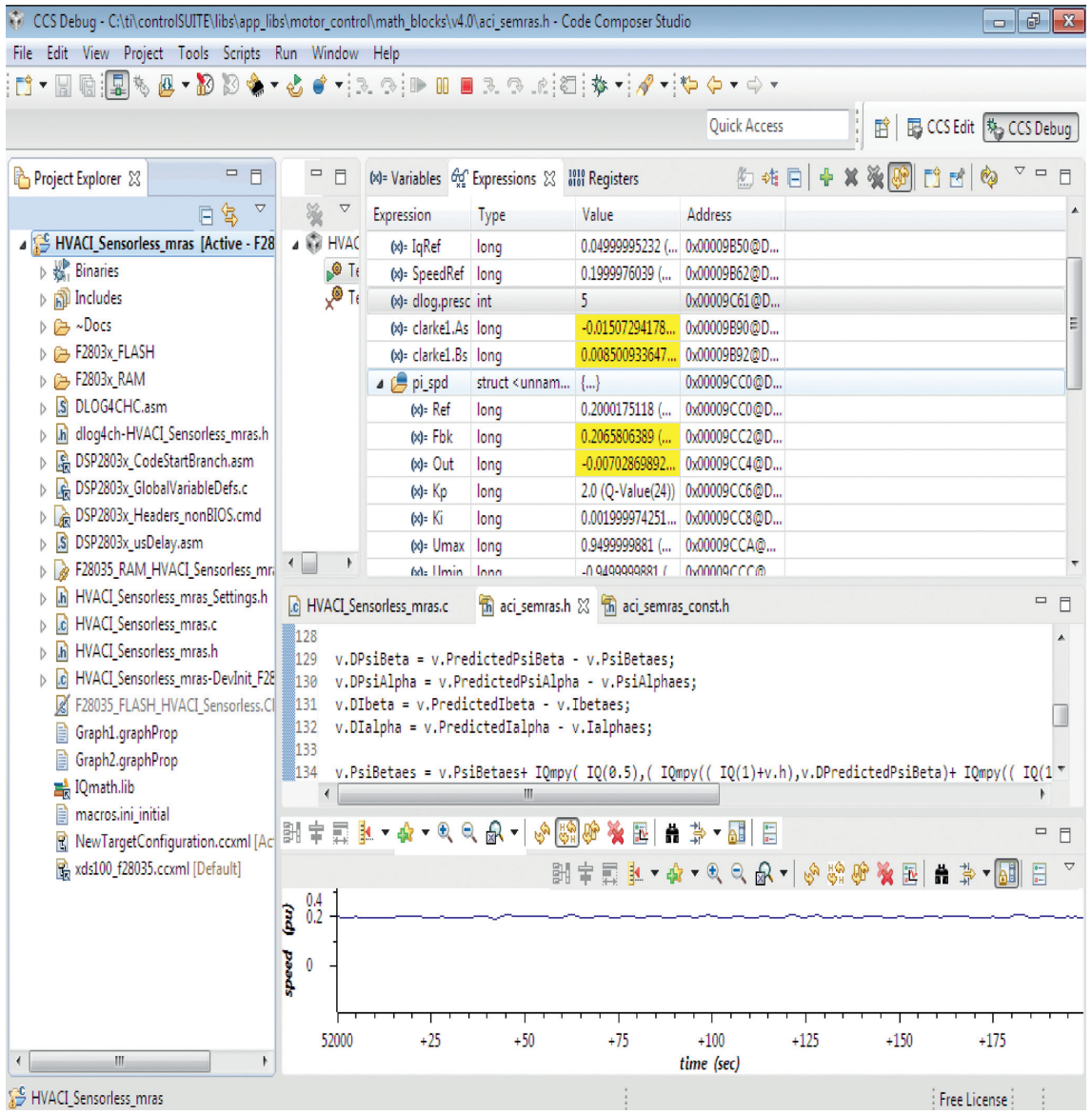

Figure 26: Snapshot of CCS programming interface while the motor is running at 0.2 pu.

host computer, which is used to program the system algorithm through Code Composer Studio v6.0. The HVDMCMTRPFC kit is connected with the host computer by a USB cable through the FTDI driver.

The source code on the host computer is debugged and loaded to the memory of the Piccolo TMS320F28035 control card through this cable. Controller power comprises of the 15 V, 5 V, and 3.3 V that the board uses to power the control card and the logic and sensing circuit present on the board. This power can be sourced from auxiliary power supply module (M2). Auxiliary power supply module (M2) can generate 15 V and 5 V DC from rectified AC. DC bus power is the high voltage line that provides voltage for the inverter stage to generate three phases of AC voltage to control the motor. [Main]-BS5 and [Main]-BS6 are the power and ground connectors for this inverter bus, respectively.

5.2. Experimental Result. The main target in this experimental investigation is to control the motor at variable speed by generating the PWM signal, which generates the appropriate sinusoidal current on the stator of the motor through DSP. This makes the motor to rotate at the required speed and control the motor at different speeds including zero speed. The six PWM output signals are shown in Figure 25 while the motor is running at 0.2 pu.

It can be seen in Figures 26 and 27 that the induction motor tracks the desired speeds well in wide ranges, which demonstrate the effectiveness of the proposed scheme. From these, the rotor speed has been a good accuracy and almost similar with that of the simulation result shown in Figure 11. The implementation result shows that the stator current-based MRAS speed estimator can estimate the rotor speed with 0.00458 pu of steady state error, and a good transient performance has been

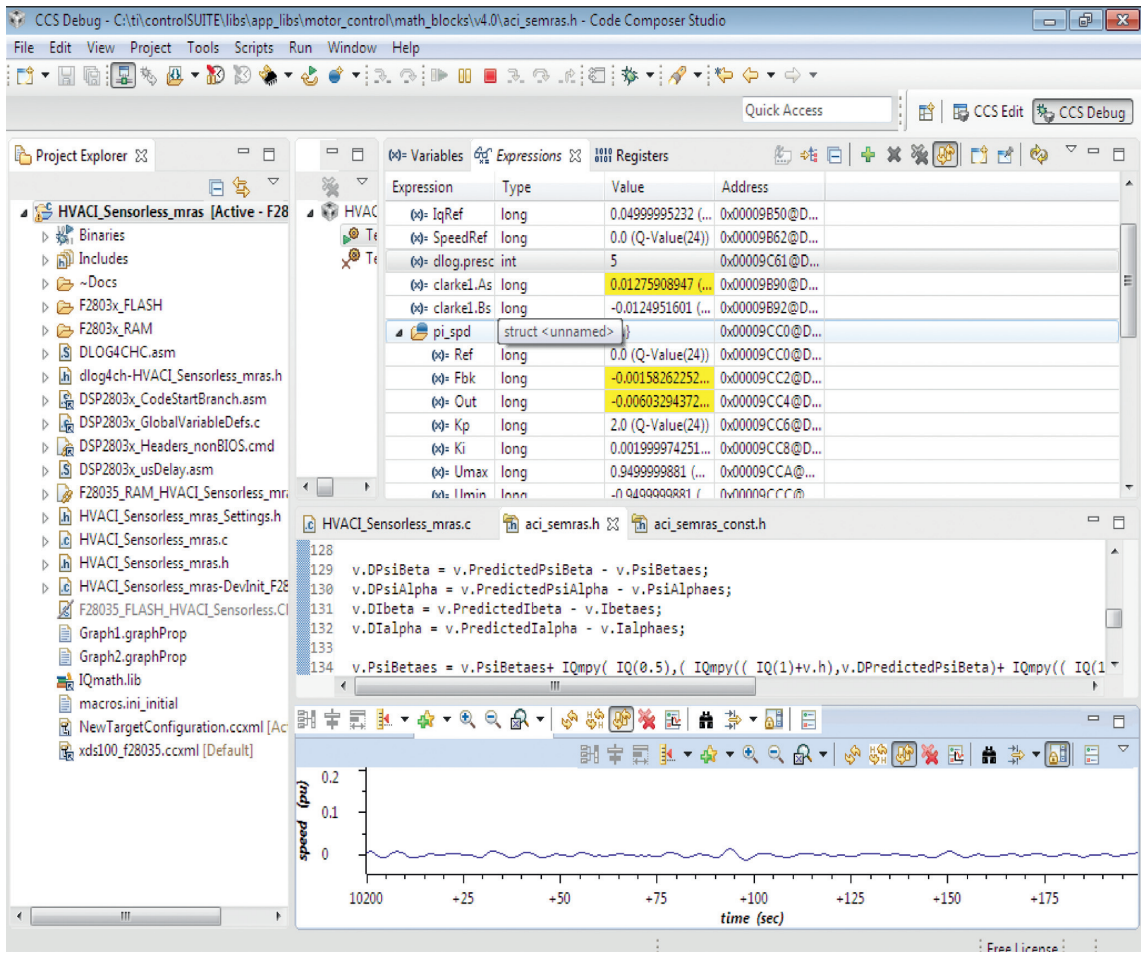

Figure 27: Rotor speed while the motor is running in a closed loop at 0.0 pu.

achieved. The implementation result shows that the stator current-based MRAS speed estimator can estimate the rotor speed with good performance of steady state and transient responses for sensorless speed control of the induction motor.

6. Conclusion

In this paper, design and implementation of the stator current-based MRAS speed estimator that overcomes the problem due to mechanical speed sensor and parameter sensitivity for speed control of IM have been investigated. The computational techniques used to simplify the stator current-based MRAS speed estimator design and its implementation on Texas instrument TMS320F28035 control card are discussed. The simulation results show that stator current-based MRAS can estimate the rotor speed with a good performance speed, and the position error of 0.024 rad/s and 0.1 rad for speed control of the induction motor has been achieved. As it is shown in Figure 8, the stator current-based MRAS speed estimator estimates the rotor speed of the induction motor with a steady state error of 0.028%, and a good transient response with rise time of less than 0.1 second and settling time 0.15 second has been achieved. The performance of the stator current-based MRAS speed estimator was analyzed in terms of speed tracking capability, torque response quickness, low speed behavior, step response of drive with speed reversal, sensitivity to motor parameter uncertainty, and speed tracking ability in the regenerative mode. The system gives a good performance at no-load and loaded condition. Hence, it can work with different load torque conditions and with parameters variation. The closed loop experimental investigation is implemented using Texas instrument, PiccoloTMS320F28035 control card. Demonstration results in smooth speed control and with a maximum steady state error of 0.00458 pu, and a good transient response has been achieved.

Data Availability

The data used to support the findings of this study are available from the corresponding author upon request.

Disclosure

The paper is driven from the author's MSc thesis, available at http://etd.aau.edu.et/handle/123456789/4862.

Conflicts of Interest

The authors declare that they have no conflicts of interest.

Acknowledgments

This work was supported by Addis Ababa University, Addis Ababa Institute of Technology in the School of Electrical and Computer Engineering.

References

[1] H. N. J. Senborg, *Control of Electrical Machine Drives*, pp. 316–345, John Wiley & Sons, Hoboken, NJ, USA, 2011.

[2] M. Zaky, "Speed sensorless control of induction motor drives (review paper)," *ACTA Electrothechnica*, vol. 49, no. 3, pp. 221–228, 2008.

[3] J. W. F. A. D. Giaouris, "Controlled AC electrical drives," *IEEE Trans. on Industrial Electronic*, vol. 55, no. 1, pp. 1–11, 2008.

[4] C. L. a. H. G. F. S. Sedghizadeh, "Sensorless speed control of switched reluctance motor drive using the binary observer with online flux-linkage estimation," *Iranian Journal of Electrical & Electronic Engineering*, vol. 5, no. 2, pp. 143–150, 2009.

[5] R. Blasco Giménez, *High Performance Sensorless Vector Control of Induction Motor Drives*, University of Nottingham, Nottingham, England, 1995.

[6] P. C. Krause and C. H. Thomas, "Simulation of symmetrical induction machinery," *IEEE Transactions on Power Apparatus and Systems*, vol. 84, no. 11, pp. 1038–1053, 1965.

[7] E. Radwan, N. Mariun, I. Aris, S. M. Bash, and A. H. Yatim, "IRFOC induction motor with rotor time constant estimation modelling and simulation," *COMPEL - The International Journal for Computation and Mathematics in Electrical and Electronic Engineering*, vol. 24, no. 4, pp. 1093–1119, 2005.

[8] K. Horváth and M. Kuslits, "Dynamic performance of estimator-based speed sensorless control of induction machines using extended and unscented kalman filters," *Power Electronics and Drives*, vol. 3, no. 1, pp. 129–144, 2018.

[9] M. Popescu, *Induction Motor Modeling for Vector Control Purposes*, Helsinki University of Technology Department of Electrical and Communications Engineering Laboratory of Electromechanics, Espoo, Finland, 2000.

[10] C. Ma, "Speed sensorless control of 3-phase induction motor using MRAS speed estimator," Theses and dissertations, Minoufiya University, Al Minufiyah, Egypt, 2003.

[11] M. N. Marwali and A. Keyhani, "A comparative study of rotor flux based MRAS and back EMF based MRAS speed estimators for speed sensorless vector control of induction machines," in *Proceedings. of the IEEE-IAS Annual Meeting*, pp. 160–166, New Orleans, LA, USA, October 1997.

[12] M. Rashed and A. F. Stronach, "A stable back-EMF MRAS-based sensorless low-speed induction motor drive insensitive to stator resistance variation," *IEE Proceedings - Electric Power Applications*, vol. 151, no. 6, pp. 685–693, 2004.

[13] F. B. a. B. B. Wafa Bourbia, "Circle-criterion based nonlinear observer design for sensorless induction motor control," in *Proceedings of the International Journal of Automation and Computing*, Annaba, Algeria, December 2014.

Hindawi
Journal of Control Science and Engineering
Volume 2020, Article ID 8347462, 15 pages
https://doi.org/10.1155/2020/8347462

Research Article

Nonzero Staircase Modulation Scheme for Switching DC-DC Boost Converter

Ayodeji Olalekan Salau,[1] **Candidus U. Eya**,[2] **and Omeje Crescent Onyebuchi**[3]

[1]*Department of Electrical/Electronics and Computer Engineering, Afe Babalola University, Ado-Ekiti, Nigeria*
[2]*Department of Electrical Engineering, University of Nigeria, Nsukka, Enugu State, Nigeria*
[3]*Department of Electrical and Electronics Engineering, University of Port Harcourt, Port Harcourt, Nigeria*

Correspondence should be addressed to Ayodeji Olalekan Salau; ayodejisalau98@gmail.com

Received 12 January 2020; Revised 24 May 2020; Accepted 2 June 2020; Published 18 July 2020

Academic Editor: Hassan Haes Alhelou

This paper presents a novel modulation scheme known as the nonzero staircase modulation scheme for switching DC-DC boost converters. This modulation scheme generates two distinct pulse trains/firing signals when a 50 Hz nonzero staircase modulating signal is compared with a 1.5 kHz triangular wave signal. Unlike the conventional modulation schemes, the proposed novel modulation scheme provides two distinctive trains of pulse-width modulated signals for mitigating low and high harmonics. It also possesses 0.56% total harmonic distortions (THD) of the output voltage waveform system, a power output of 4591 W, and THD of 1.12% in the DC-DC boost converter system. It has a simple design and low power loss of 209 W. The proposed scheme enables the single switch boost DC-DC converter used to have an efficiency of 96%. The proposed scheme can be applied in single switch or double switch boost DC-DC converter based-hospital equipment.

1. Introduction

The DC-DC boost converter is a power electronic converter that is placed most especially between a low unregulated voltage power source and a load. Its key function is to step up low voltage power sources to suit the needed application. Some areas of application of DC-DC boost converters are in DC microgrid systems, pulsed lasers, electric trains, X-rays, uninterruptible power systems, inverters, satellites, and wireless power transfers [1]. In the course of its application, it can change an unregulated fixed voltage as in the case of a battery or variable voltage to a controlled variable output voltage depending on the level of the duty cycle (D) [2]. Its input voltage sources could be obtained from solar power supplies, rectified AC voltage supplies, battery, fuel cells, biomass, and supercapacitors [3]. It consists of three non-storage elements (power electronic switch, freewheeling diode, and power diode), and two storage elements, inductor and capacitor. The DC-DC boost converter can operate both in continuous current mode (CCM) and discontinuous current mode (DCM) based on its area of application.

In switched mode condition, power is transferred from the source to the load by triggering power electronic switches such as MOSFETs or IGBTs. A number of works have been presented on different modulation schemes used in firing different DC-DC boost converters [4, 5]. Some of them are Single pulse-width modulation, multiple pulse-width modulation (MPWM), DC/triangular compared modulation scheme, square-wave modulation, and many others with their merits and demerits [6, 7]. In single pulse-width modulation, there is only one pulse in each half cycle and the width of the pulse is varied to control the output voltage of the converter. Moreover, in this type of PWM scheme, a carrier signal is compared with a square reference wave. The frequency of the carrier is twice the frequency of the reference signal. The triangular wave has a constant amplitude and the square reference wave has a variable amplitude, so that the width of the pulse can be varied to eliminate low harmonic distortion. The major demerit of this scheme is that as the pulse width increases, it contributes heavily to switching losses, increases the harmonic content, and decreases efficiency. In MPWM, many pulses of the

same width are produced in each half cycle and the greater harmonic contents can be reduced unlike in the single pulse-width modulation. In a square-wave modulation, one pulse is generated in one-half cycle with a width of 50% of the full cycle. This is formed when a reference sine wave is compared with a zero input potential voltage. It only reduces the low harmonic distortions and pushes the high harmonic distortions to large discrete output filter components. This also increases the cost of production, weight, and the volume of the system.

A conventional staircase modulation scheme as presented in [8] was applied in controlling a hybrid multilevel inverter topology with a reduced number of power electronic components. In [9], another zero crossing digital staircase pulse modulator was used in maximizing the fundamental component and eliminating certain low harmonics in DC/AC converters. Apart from considering only low harmonics, a complex computational analysis was also analysed.

In this paper, a novel modulation scheme known as nonzero staircase modulation scheme with simplified analysis for switching DC-DC boost converters is proposed. It has two distinctive trains of pulse width features for mitigating both low and high harmonic distortions (total harmonic distortion) for power loss reduction in power electronic systems. The proposed modulation scheme is used for single-switched PWM DC-DC boost converters but can also be applied in double-switched DC-DC converters.

The major advantages of the proposed scheme are as follows: (i) it minimizes the cost of using high system filter components since it has the capability of mitigating both low and high harmonics. (ii) It enables the DC-DC boost converter system to experience low power losses. (iii) It increases the quality of output power due to its low total harmonics distortions. (iv) It has a simple design. (v) It assists the DC-DC converter in operating in a continuous current mode. (vi) It enhances high power system efficiency.

2. Single-/Double-Switched DC-DC Converter Modulation Schemes

The efficiency enhancement of DC-DC boost converters by parallel switch correlation (connection) was carried out by the authors in [10]. The single switch used in their work is triggered by a uniform 25 kHz pulse. The 25 kHz firing pulse was obtained with the aid of an Arduino UNO microcontroller which achieved a conversion efficiency of 70%. However, the uniform pulses generated can only minimize low harmonics. Many DC-DC converter topologies were reviewed by authors in [11] based on their different degrees of efficiencies. Meanwhile, only circuit configuration modulation schemes which also contribute greatly to the efficiency of DC-DC converters were not considered by the authors in their work.

Therefore, considering the modulation techniques used in single switch DC-DC converters/double switch DC-DC converters, the most common ones used are DC voltage compared with Sawtooth modulation scheme (DCVCSM)/chaotic frequency modulation [12], DC voltage-triangular based modulation scheme (DCVTBM), zero potential compared sinewave modulation scheme (ZPCSMS), rectified-triangular modulation scheme (RTMS), and sliding window-based pulse-width modulation (SWBPWM) [13–18]. RTMS can also be applied in a converter with more than one switch converter [19].

A rectified-triangular modulation scheme (RTMS) is presented in Figure 1(a). It produces the pulses in Figure 1(b), while Figure 1(c) illustrates the power output and its spectral analysis. A power output of 2928 W, total harmonic distortion (THD) of 9.79%, and a modulation index of 0.9 was realized using the RTMS technique on the boost DC-DC converter in Figure 2.

The DC-voltage compared with Sawtooth modulation (DCVCSM) scheme is shown in Figure 3(a). The pulses generated by comparing DC voltage and Sawtooth signal (ZPCSMS) is shown in Figure 3(b), while Figure 3(c) shows the spectral analysis of output power of the boost DC-DC converter using DCVCSM.

The DCVTBM technique and its generated triggering pulses are shown in Figures 4(a) and 4(b). The harmonic analysis of the power output of the boost DC-DC converter using DCVTBM is presented in Figure 4(c). It can be seen that Figure 4(c) contains a DC output power and THD of 4204 W and 4.65%, respectively. The DCVTBM possesses a modulation index of 0.9.

A sinusoidal reference voltage is compared with a zero potential difference as shown in Figure 5(a). This produces the switching pulses in Figure 5(b). The pulses generated were used to switch the circuit in Figure 2 in order to generate the DC power output waveform shown in Figure 5(c). From the spectral analysis illustrated in Figure 5(c), it is observed that a DC power output and THD of 2229 W and 33.74% was achieved, respectively.

3. Principle and Design Method for Generating the Nonzero Staircase Modulation

The nonzero staircase modulation scheme is a type of modulation scheme that generates two distinct pulse trains/firing signals when a nonzero staircase modulating signal is compared with a triangular wave signal. In this type of modulation technique, the wider section of the generated pulses reduces the low order harmonics, while the narrower region minimizes the higher-order harmonics. The number of the nonzero staircase modulating signal has ascending and descending regions. The descending region is a mirror image of the ascending region. The height of the modulating signal is equivalent to the amplitude of the voltage signal. Overmodulation occurs when the nonzero staircase reference is greater than the carrier wave. Therefore, the modulating nonzero staircase signal should be less than the carrier wave.

To design this, a mode of half-sine wave is needed to be partitioned into equal parts following other designer's considerations. In this work, a mode of half-sine wave was partitioned into twenty equal parts with time scales. The peak at each point is relative to the switching angle at that position. In order to actualize the nonzero position of the

proposed staircase scheme, the zero angle and 180° are not used in the design. In addition, an offset level, h_o is chosen. The key idea here is to ensure complete avoidance of discontinuous current mode and to accomplish high harmonic reduction (in either low and high order harmonics or total harmonic reductions). The total number, N, of the proposed system should be an even number. The height of the nonzero staircase is equivalent to the signal voltage. The proposed schemes design is presented in Figure 6.

In Figure 6, it is observed that the heights of staircase reference from h_{11} to h_{20} are the mirror images from h_1 to h_{10}. This simply means that $h_1 = h_{11}$, $h_2 = h_{12}$, $h_3 = h_{13}$, $h_4 = h_{14}$, $h_5 = h_{15}$, $h_6 = h_{16}$, $h_7 = h_{17}$, $h_8 = h_{16}$, $h_9 = h_{19}$, and $h_{10} = h_{20}$.

The switching angles, θ_i, for 20 steps of the staircase are calculated using the formula in equation (1) and the results are presented in Table 1.

$$\theta_i = \frac{J \times 180}{2N}, \tag{1}$$

where J is an odd number, i.e., 1, 3, 5, 7, 9, 11, 13, 15, 17, 19, and N is the total number of steps. $i = 1, 2, 3, 4, 5, 6, \ldots 20$.

3.1. Computation of Switching Angles. Using equation (1), where N is 20, Table 1 is obtained.

For $i = 1$ and $J = 1$, θ_1 is obtained as $\theta_1 = (1 \times 180)/(2 \times 20) = 4.5^\circ$.

The height of each staircase signal from the zero-axis is H_i and is determined using the following equation:

$$H_i = A_p \cos(\theta_i - 90), \tag{2}$$

where $i = 1, 2, 3, \ldots\ldots\ldots 20$.

3.2. Computation of Heights of Staircase Modulating Reference Signal from Zero X-Axis. The heights of staircase modulating Reference Signal from Zero X-axis; H_i are computed using equation (2) as follows:

$$H_i = A_p \cos(\theta_i - 90), \tag{3}$$

For $i = 1$ and using the calculated value of $\theta_1 = 4.5^\circ$, assuming $A_p = 10$ m throughout the process, then

$$H_1 = 10 \cos(4.5 - 90) = 0.78 \text{ m}. \tag{4}$$

The remaining heights of the staircase modulating reference signal from the zero-axis were computed and are presented in Table 2.

The height of each staircase signal from the nonzero-axis is h_i and is calculated using

$$h_i = \left[A_p \cos(\theta_i - 90)\right] - h_o = H_i - h_o. \tag{5}$$

3.3. Computation of Heights of Nonstaircase Modulating Reference. The offset, h_o, is assumed to be 0.05 m throughout the calculation of h_i. Therefore, for $H_1 = 0.78$ m as calculated, and $h_o = 0.05$ m,

$$h_1 = 0.78 - 0.05 = 0.73 \text{ m}. \tag{6}$$

The other heights of the nonstaircase modulating reference signal were obtained and are presented in Table 3.

Having computed h_1, $h_2, h_3, h_4, h_5, h_6, h_7, h_8, h_9$, and h_{10} of the nonzero staircase modulation scheme, we obtain h_{11}, $h_{12}, h_{13}, h_{14}, h_{15}, h_{16}, h_{17}, h_{18}, h_{19}$, and h_{20} as the mirror images of $h_1, h_2, h_3, h_4, h_5, h_6, h_7, h_8, h_9$, and h_{10}.

The complete computed results of equations (1), (2), and (5) for the generating nonzero staircase reference signal with their Θ_i, H_i, and h_i mirror image values which were used in MATLAB/Simulink modulating block shown in Figure 7 are presented in Table 4.

The carrier signal is generated in Matlab/Simulink using the following equation:

$$C_r = \begin{bmatrix} \frac{1}{f_c} & -\frac{1}{f_c} & \frac{1}{2f_c} & \frac{1}{f_c} \\ y - M & y & y - M & \end{bmatrix}, \tag{7}$$

where C_r is the carrier signal, f_c is the carrier frequency, y is the amplitude of the carrier wave, and M is an integer. In equation (7), "y" must be equal to "M" in magnitude. In order to produce the triggering signals with two distinctive pulse trains for firing the IGBT switch connected in the DC-DC boost converter, equation (2) is compared with equation (5).

The values of the storage elements L and C of the DC-DC boost converter are computed using equations (8) and (9) as given in [2].

$$L_{\min} = \frac{D(1 - D)^2 R}{2f_c}, \tag{8}$$

$$C_{\min} = \frac{D}{R(\Delta V_o / V) f_c}. \tag{9}$$

$L_{\min}$, $C_{\min}$, V_o, and R are the minimum capacitance, minimum inductance, output voltage, and output load resistance of the converter.

4. The Feedback Control System

4.1. Circuit Diagram of the PI Controller. In the feedback control unit, the proportional-plus-integral controller is utilized [10–12]. The circuit diagram is shown in Figure 8 [20–22]. The figure shows the circuit diagram of the PI controller with the following components, sensed voltage, V_{sensed}, DC referenced voltage, V_{ref1}, error voltage (input voltage to the PI controller), V_e, resistances, R_1, R_2, R_3, R_4, R_5 and feedback capacitance, C.

The transfer function of the PI controller in Figure 8 is expressed as follows [23]:

$$T(s) = \frac{V_{\text{out}}}{V_e} = K_p + \frac{K_i}{s}. \tag{10}$$

4.2. Tuning Principle of the PI Controller. The PI controller is tuned or adjusted based on the level of the output voltage across the load connected to the DC-DC boost converter.

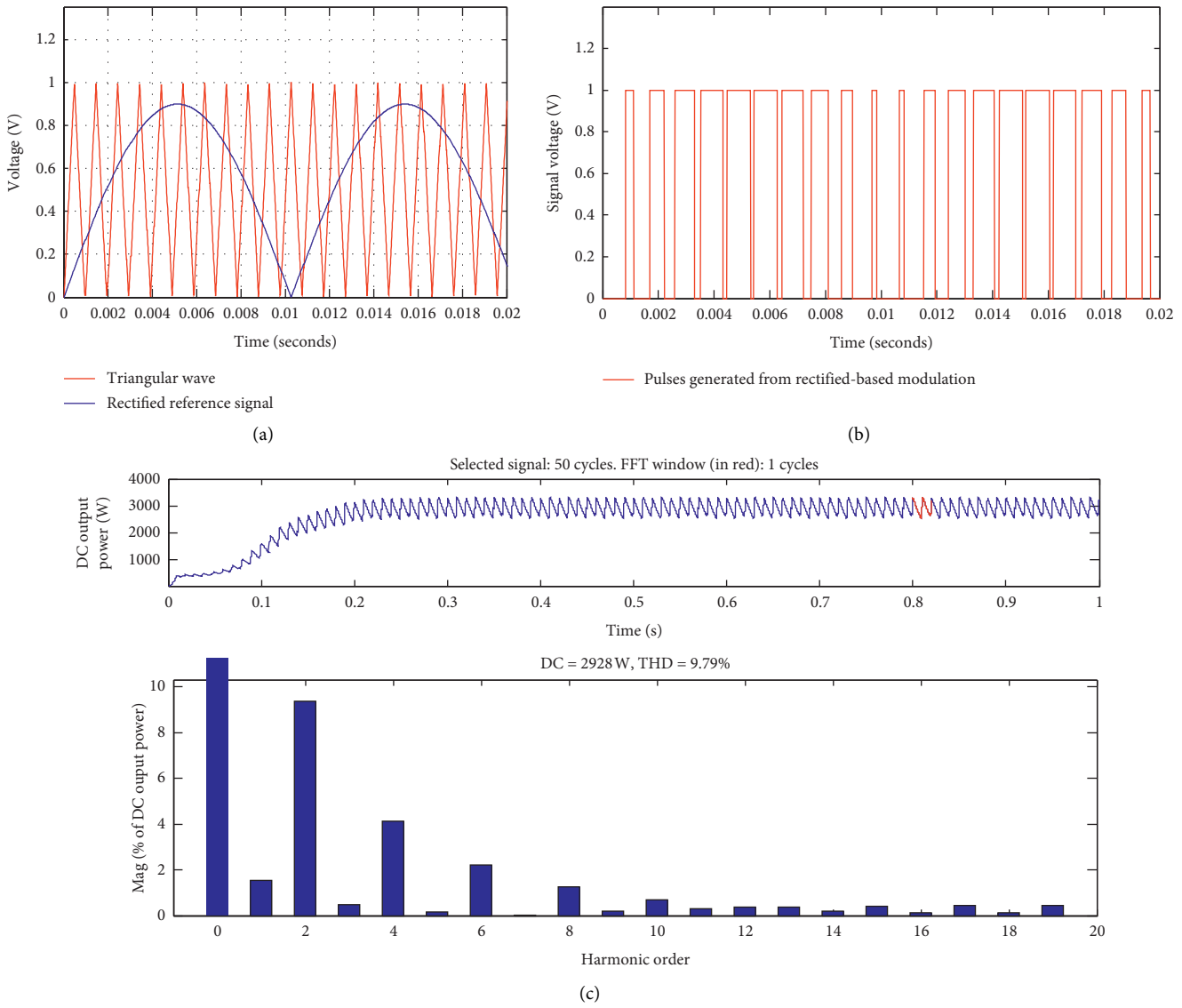

Figure 1: (a) RTMS. (b) Firing pulses of RTMS. (c) Spectral analysis of the output power of boost DC-DC converter using RTMS.

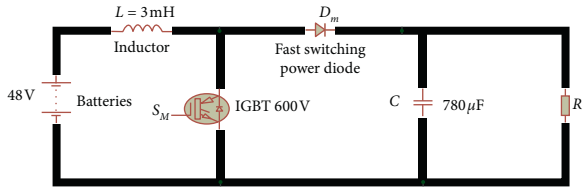

Figure 2: Proteus Circuit of DC-DC boost converter [13].

This was done to keep the output voltage constant. The PI tuning principle is stated as follows:

$$V_e = \begin{cases} V_{\text{sensed}} - V_{ref1}, & \text{when } V_{\text{sensed}} > V_{\text{ref1}}, \text{ then PI decreases the } W1 \text{ and } W2 \text{ in Figure 9 (b)}, \\ V_{\text{ref1}} - V_{\text{sensed}}, & \text{when } V_{\text{sensed}} < V_{\text{ref1}}, \text{ then PI increases the } W1 \text{ and } W2 \text{ in Figure 9 (b)}, \\ 0, & \text{when } V_{\text{sensed}} = V_{\text{ref1}}, \text{ then } W1 \text{ and } W2 \text{ in Figure 9 (b) remain constant.} \end{cases} \quad (11)$$

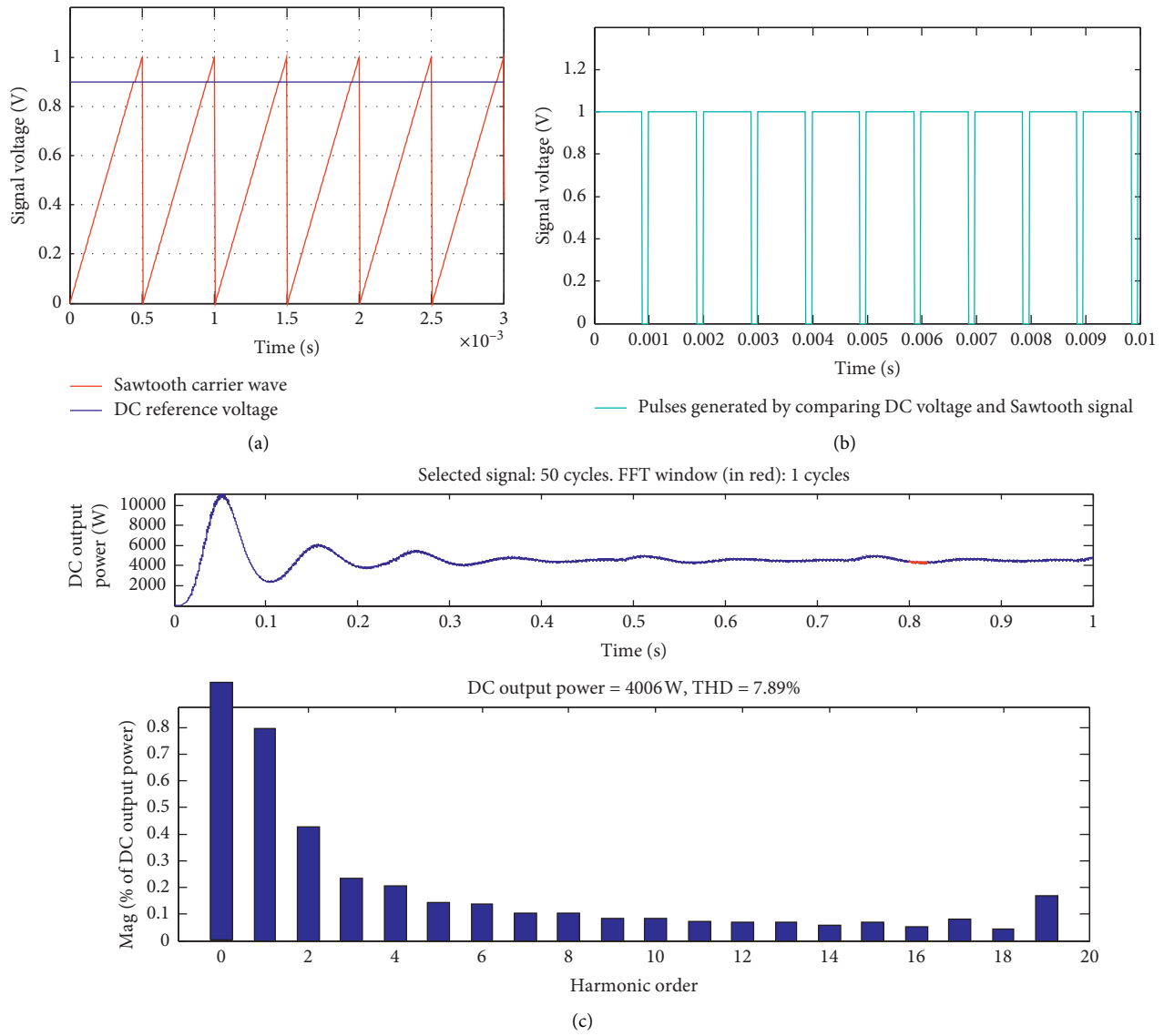

Figure 3: (a) DCVCSM. (b) Firing pulses of ZPCSMS. (c) Spectral analysis of the output power of boost DC-DC converter using DCVCSM.

When the sensed voltage is greater than the DC reference voltage, it means that the output voltage at that point in time is greater than the desired output voltage of the system; then, the error voltage goes into the PI controller. Immediately after this, the current will flow from the capacitor, C, to V_{ref1} through R_5, R_3, and R_2 to discharge the capacitor. As the capacitor, C, discharges, the width of switching signals, $W1$ and $W2$ are reduced to bring back the output voltage to the desired output voltage level. On the other hand, if the sensed voltage is lower than the DC reference voltage, it means that the output voltage at that moment is lower than the desired output voltage of the system; then, the error voltage goes into the PI controller to increase the width of switching signals, $W1$ and $W2$, making the power switch to operate faster. During this period, the current flows from V_{ref1} to charge the capacitor through R_2, R_3, and R_5. Furthermore, if V_{sensed} is equal *to* V_{ref1}, the error voltage becomes zero. When no current flows into or out of the PI controller, the voltage across the capacitor, C, clamps the widths of the pulses. At this point, the output voltage across the load becomes stabilized. The electrical interactions of V_e, V_{out}, R_2, R_3, C, and R_5 produce the proportional constant, K_p, and integral constant, K_i that controls the switching action in order to stabilize the output voltage of the system.

4.3. Determination and Computation of Proportional Constant and Integral Constant of the PI Controller. The proportional and integral terms K_p and K_i used in this work are deduced as follows:

Considering the inverting terminal of the operational amplifier in Figure 8 and applying the Kirchhoff's current law, the current entering node L is equal to the current leaving it; therefore,

$$\frac{V_e - V_L}{R_3} = \frac{V_L - V_{\text{out}}}{R_5 + Z_C}, \tag{12}$$

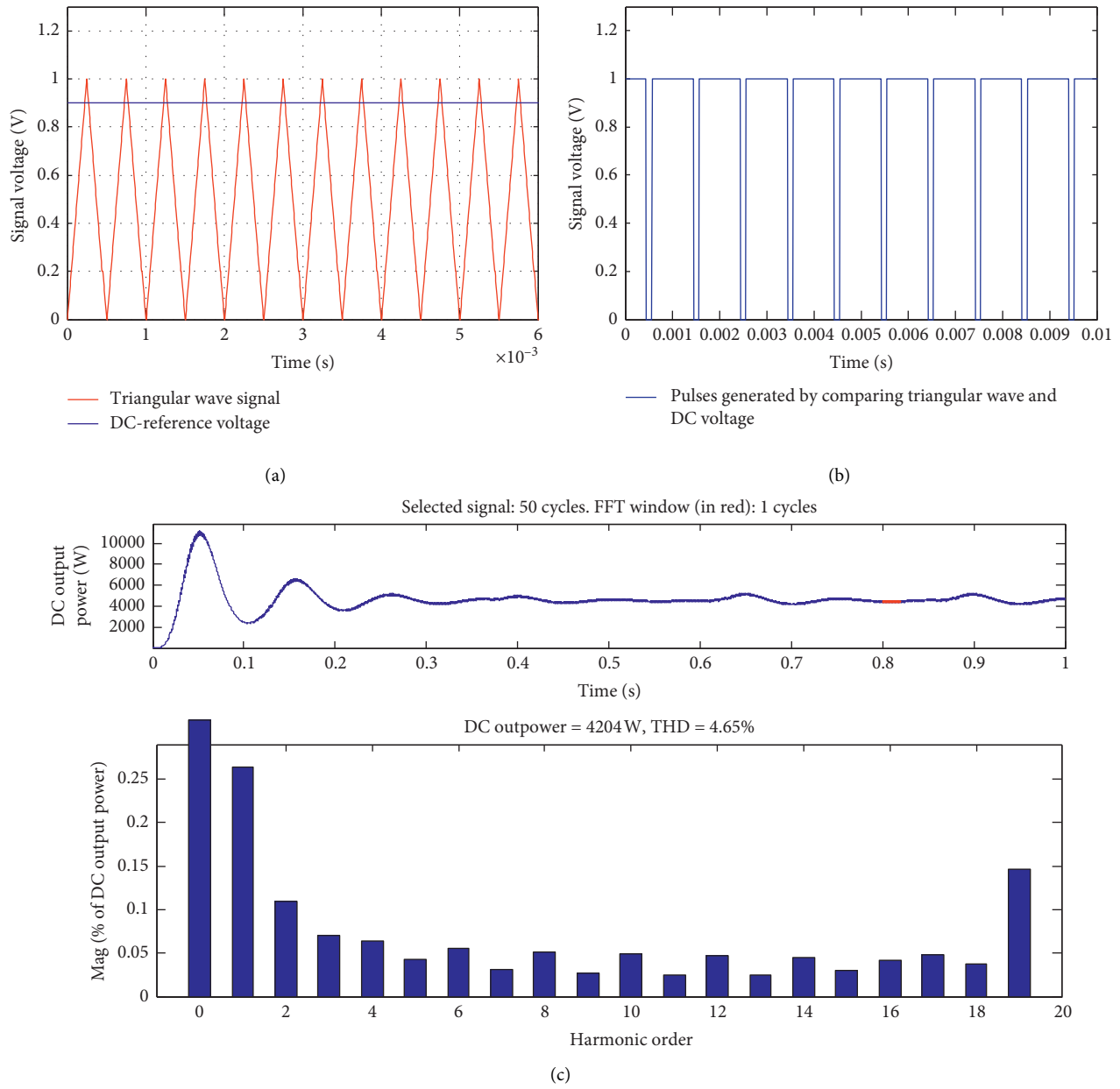

FIGURE 4: (a) DCVTBM. (b) Firing pulses of ZPCSMS. (c) Spectral analysis of the output power of boost DC-DC converter using DCVTBM.

where V_L and Z_C are the inverting terminal voltage and capacitive impedance, respectively. Therefore, by rearranging equation (12) to make V_L the subject of the formula, equation (13) is obtained.

$$V_L = \frac{V_e R_5 + V_e Z_C + R_3 V_{\text{out}}}{R_3}. \tag{13}$$

Furthermore, considering the noninverting terminal and node, m, the noninverting voltage becomes

$$V_m = 0. \tag{14}$$

Then, equating equations (13) and (14), and getting the ratio of V_{out} to V_e of the PI controller and taking its absolute expression, equations (15) and (16) become

$$\left|-\frac{V_{\text{out}}}{V_e}\right| = \left|\frac{R_5 + Z_C}{R_3} = \frac{R_5}{R_3} + \frac{Z_C}{R_3}\right|, \tag{15}$$

$$\frac{V_{\text{out}}}{V_e} = \frac{R_5}{R_3} + \frac{1}{R_3 C s}. \tag{16}$$

Subsequently, comparing equations (10) and (16), the K_p and K_i becomes

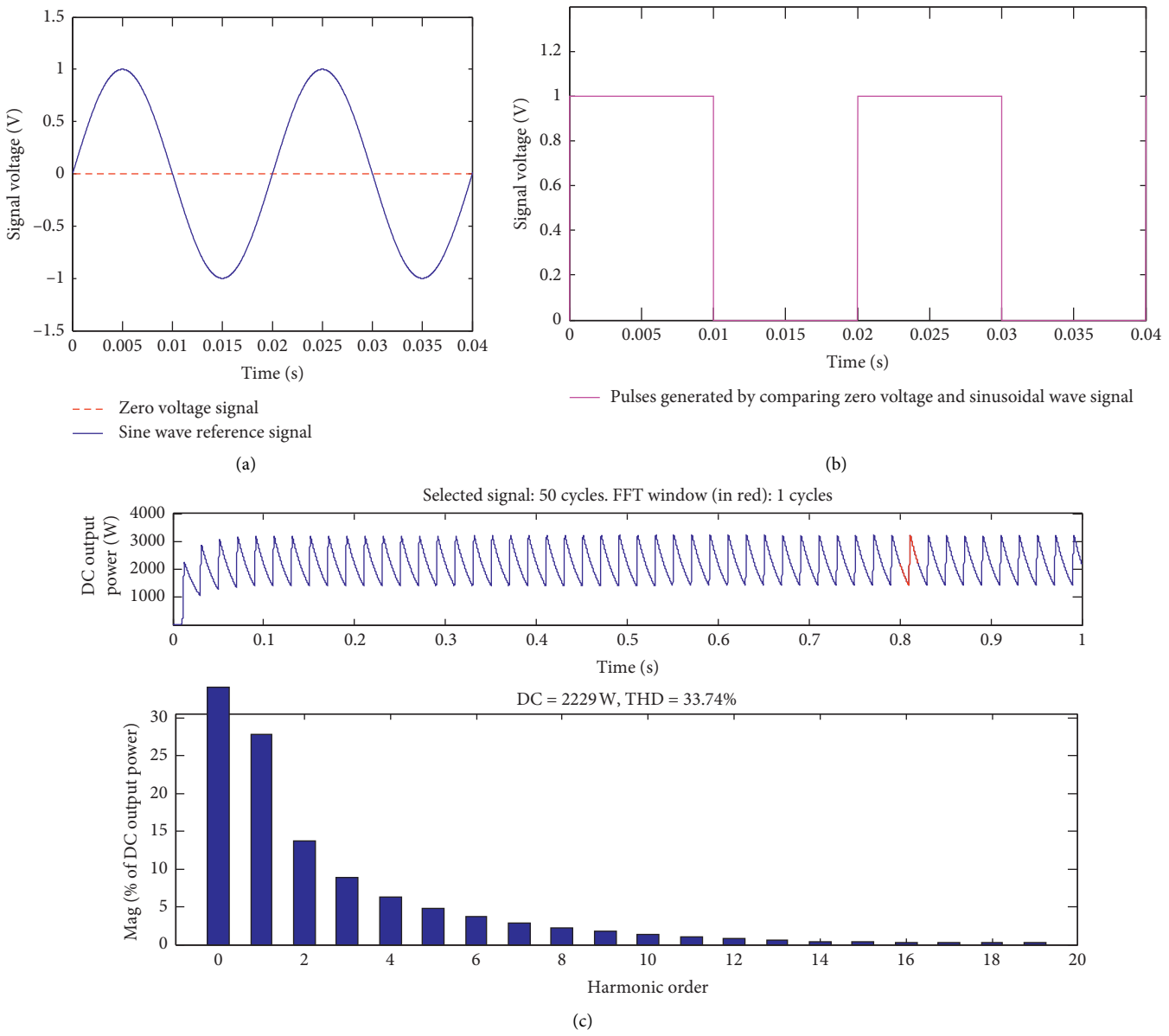

Figure 5: (a) ZPCSMS. (b) Firing pulses of ZPCSMS. (c) Spectral analysis of the output power of boost DC-DC converter using ZPCSMS.

$$K_p = \frac{R_5}{R_3}, \tag{17}$$

$$K_i = \frac{1}{R_3 C}. \tag{18}$$

Moreover, the time constant for charging and discharging the feedback capacitor in Figure 8 is expressed by the following equation:

$$\tau = R_3 C, \tag{19}$$

where τ is the time constant for charging and discharging, C. Assuming that $R_5 = R_3 = 10\text{k}\Omega$, and $\tau = 1.74$ seconds. Substituting the values of R_3 and τ in equation (19), then, C becomes 174 μF. Then substituting the values of C and R_3 in equation (18), K_i becomes 0.57. When the values of R_3 and R_5 are substituted in equation (17), K_p becomes 1.0.

5. Total Harmonic Distortion

5.1. Computational Formula of Total Harmonic Distortion. The current and voltage of total harmonic distortions (THDs) are computed using the expressions in the following equations [2, 24]:

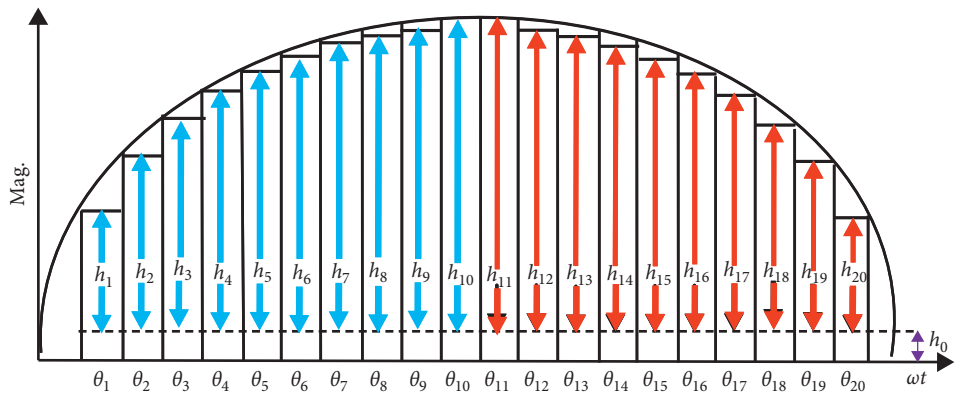

Figure 6: Design scheme for the nonzero staircase reference.

Table 1: Calculation of switching angles.

S/n	i	J	θ
1	1	1	$\theta_1 = 4.5^o$
2	2	3	$\theta_2 = 13.5^o$
3	3	5	$\theta_3 = 22.5^o$
4	4	7	$\theta_4 = 31.5^o$
5	5	9	$\theta_5 = 40.5^o$
6	6	11	$\theta_6 = 49.5^o$
7	7	13	$\theta_7 = 58.5^o$
8	8	15	$\theta_8 = 67.5^o$
9	9	17	$\theta_9 = 76.5^o$
10	10	19	$\theta_{10} = 85.5^o$

Table 2: Calculation of heights of staircase modulating reference signal from zero-axis.

S/n	i	θ	H_i (m)
1	1	$\theta_1 = 4.5^o$	$H_1 = 0.78$
2	2	$\theta_2 = 13.5^o$	$H_2 = 2.33$
3	3	$\theta_3 = 22.5^o$	$H_3 = 3.82$
4	4	$\theta_4 = 31.5^o$	$H_4 = 5.22$
5	5	$\theta_5 = 40.5^o$	$H_5 = 6.49$
6	6	$\theta_6 = 49.5^o$	$H_6 = 7.60$
7	7	$\theta_7 = 58.5^o$	$H_7 = 8.53$
8	8	$\theta_8 = 67.5^o$	$H_8 = 9.72$
9	9	$\theta_9 = 76.5^o$	$H_9 = 9.72$
10	10	$\theta_{10} = 85.5^o$	$H_{10} = 9.96$

$$\text{THD (for current)} = \frac{\sqrt{\sum_{n=2}^{\infty} I_n^2}}{I_1}, \tag{20}$$

$$\text{THD (for voltage)} = \frac{\sqrt{\sum_{n=2}^{\infty} V_n^2}}{V_1}, \tag{21}$$

where I_n and V_n are amplitude harmonic components of the current, I_1, and the voltage, V_1.

Table 3: Computation of heights of nonstaircase modulating reference.

S/n	i	H_i (m)	h_i (m)
1	1	$H_1 = 0.78$	$h_1 = 0.73$
2	2	$H_2 = 2.33$	$h_2 = 2.28$
3	3	$H_3 = 3.82$	$h_3 = 3.77$
4	4	$H_4 = 5.22$	$h_4 = 5.17$
5	5	$H_5 = 6.49$	$h_5 = 6.44$
6	6	$H_6 = 7.60$	$h_6 = 7.55$
7	7	$H_7 = 8.53$	$h_7 = 8.03$
8	8	$H_8 = 9.72$	$h_8 = 9.19$
9	9	$H_9 = 9.72$	$h_9 = 9.67$
10	10	$H_{10} = 9.96$	$h_{10} = 9.92$

The computation of THD current and voltage waveforms using equations (18) and (19) is an approximate method presented in [23]. This method was found to be a very cumbersome, difficult, and time-consuming [23]. Therefore, to save time and get precise values of THD of the system, we employed a tool known as power graphic user interface Fast Fourier Transform, PGUIFFT, or power graphic user interface analysis tool, PGUIAT in Matlab/Simulink environment, 2014.

5.2. Steps in Using Power Graphic User Interface Fast Fourier Transform

Step A: configure the proposed system in the Simulink environment.

Step B: select the PGUIFFTAT from the Simulink library browser.

Step C: double click on workspace block and single click on "parameters" inside the workspace. Then click on "History" and adjust its "Format" in "Structure with time" and click "OK."

Step D: run or simulate the proposed system.

Step E: double click on PGUIFFTAT discrete block, it will display "simulation and configuration Option."

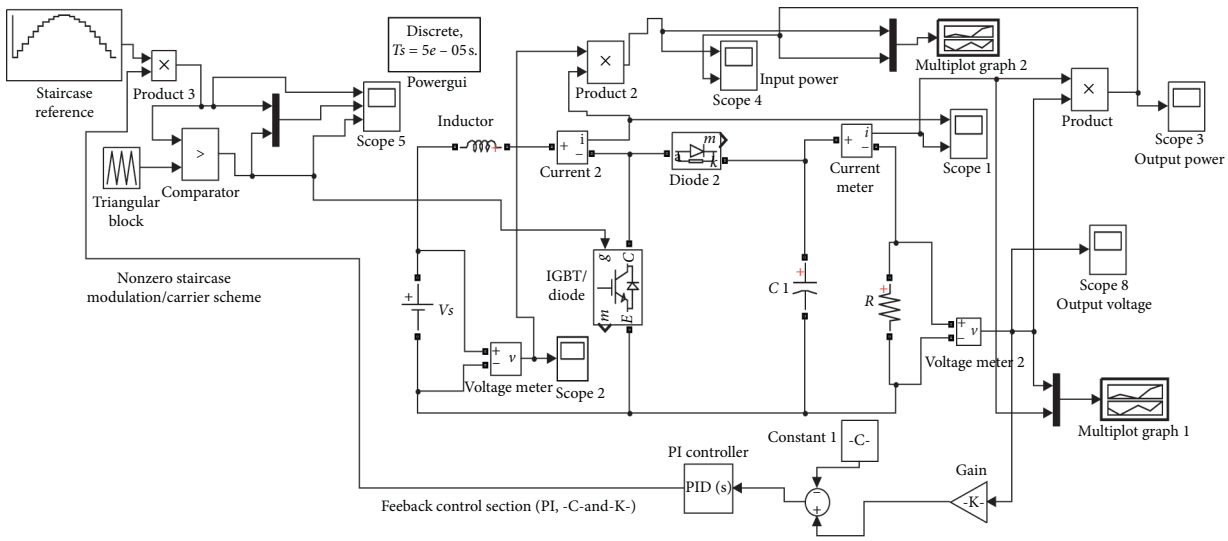

Figure 7: MATLAB/simulink model of the proposed system.

Table 4: Computed values for nonzero staircase modulation scheme.

Serial number (i)	Θ_i (°C)	H_i (m)	h_i (m)
1	4.50	0.78	0.73
2	13.50	2.33	2.28
3	22.50	3.82	3.77
4	31.50	5.22	5.17
5	40.50	6.49	6.44
6	49.50	7.60	7.55
7	58.50	8.53	8.03
8	67.50	9.24	9.19
9	75.50	9.72	9.67
10	85.50	9.97	9.92
11	85.50	9.97	9.92
12	75.50	9.72	9.67
13	67.50	9.24	9.19
14	58.50	8.53	8.03
15	49.50	7.60	7.55
16	40.50	6.49	6.44
17	31.50	5.22	5.17
18	22.50	3.82	3.77
19	13.50	2.33	2.28
20	4.50	0.78	0.73

Step F: single click on "FFT analysis;" it will display four subsections: signal section, FFT analysis section, available signal section, and FFT setting section.

Step G: finally, click on the display button; the FFT analysis section, it will show the total harmonic distortion level of the output wave in percentage value and in bar chart form.

6. Boost DC-DC Converter Power Circuit and Its Efficiency

The DC-DC boost converter circuit used in this work is shown in Figure 2. It is the power circuit where the nonzero staircase modulation scheme is applied. It operates as follow: during the positive first half cycle, as soon as the power electronics switch, S_M is ON, the fast switching power diode, D_m will switch OFF, and then the magnetic energy flows linearly at the input storage device, L. At this moment, load, R depends solely on the electric energy stored in the capacitor, C. During the negative half cycle, the switch S_M is turned OFF which alternately sets D_m ON. At this point, the already stored magnetic energy in L discharges to charge C to feed the Load. A similar process takes place during other cycles.

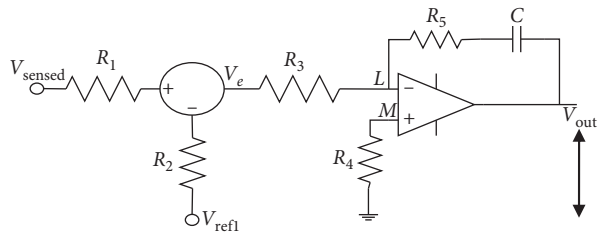

Figure 8: Circuit diagram of a proportional-plus-integral controller.

Efficiency, ε, of the converter can be defined as the ratio of power output, P_o, of the converter to its power input, P_s, expressed in percent [25].

$$\varepsilon = \frac{P_o}{P_s} * 100. \tag{22}$$

The parameters used in the power circuit, frequencies, and feedback system of this work are listed in Table 5, while the parameters of the proposed system are shown in Table 4. Table 5 also contains the output power of the DC-DC converter using the proposed modulation scheme.

The MATLAB Simulink block and the control unit of Figure 2 are shown in Figure 7. Figure 7 consists of the staircase modulation scheme, power circuit, Simulink

Table 5: Parameters used in the proposed system.

Parameter	Ratings
Duty cycle and load resistance	0.90 and 50 Ω
Capacitance, C	780 μF
Input inductance, L	3 mH
Input and output voltages, vs and V_o	48 V and 500 V
Power IGBT switch	600 V, 160 A
Power diode	1000 V
Switching and reference frequencies	1.5 kHz and 50 Hz
Proportional and integral values	1.0 and 0.57
Output power	4591 W

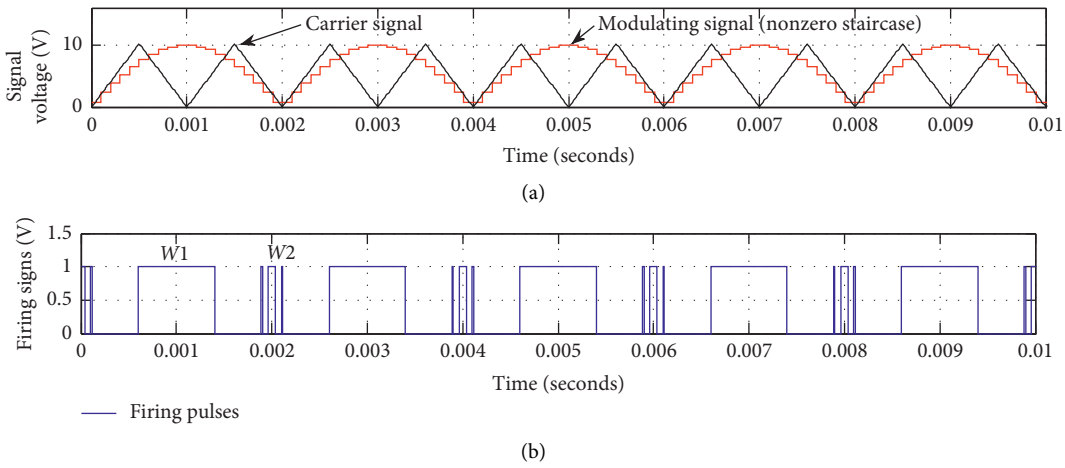

Figure 9: Nonzero staircase modulation scheme.

measuring blocks, and negative control feedback. The control feedback is made up of voltage sensors, dc-negative reference, and PI controllers.

7. Simulation Results

This work was simulated in MATLAB/Simulink 2014 environment. Figure 9(a) shows a comparison of triangular waves (carrier signal), C_r, with nonzero staircase reference, (NZSR) waveform. It was observed that when NZSR is greater than C_r, a firing pulse is formed as shown in Figure 9(b). Figure 9(b) displays two distinctive trains of pulses with different pulse widths. The pulse at the position of $W1$, reduces the low order harmonic distortions, whereas the pulse at the position of $W2$ in Figure 9(b) mitigates the high order harmonics in the proposed system. The pulses in Figure 9(b) are used to trigger the IGBT switch, S_M, in Figures 2 and 7 before any output waveform can be produced.

In Figure 10(a), a plot of the source voltage of 48 V versus time is illustrated, while in Figure 10(b), the current flowing through the inductor, L, is displayed. The transient stage of the current occurred at a time duration of $0 \le t \le 0.5$ seconds with the highest current value of 150 A. The current waveform later stabilized at $0.5 \le t \le 1$ seconds at a currentof 100 A with some ripples.

The output voltage and current versus time of the proposed system are plotted in Figures 10(a) and 10(b) respectively. The results show that oscillations occur in the waveforms between zero (0) seconds and 0.5 seconds until they are stabilized immediately after 0.5 seconds with a voltage and amplitude of 480.3 V and 9.56 A respectively.

The characteristic performance of the output voltage and current are illustrated in Figures 11(a) and 11(b). The transient and steady states occurred at $0 \le t \le 0.031$ seconds and $0.54 \le t \le 1$ seconds.

The power input and output of the DC-DC boost converter of the proposed system are plotted against time in Figures 12(a) and 12(b). In Figure 12(a), at $0 \le t \le 0.031$ seconds, the power input rises to 8000 W and at $t = 0.18$ seconds, it sharply dropped down to 6000 W. Then between 0.0321 seconds and 0.5 seconds, it fluctuates at different ratings due to the unstable state of the system during the transient stage. Beyond 0.5 seconds, the power input is stabilized at 4800 W throughout the operation. Figure 12(b) shows that during the transient stage, the power output did not drop sharply, rather it reached its peak point (60015 W) and finally stabilized at 4591 W. The stabilization of the output power and also that of current and voltage were due to the proportional integral (PI) controller incorporated in the system. The results show that under steady state operation of the system, a power loss of 209 W and an efficiency of 96% is realized.

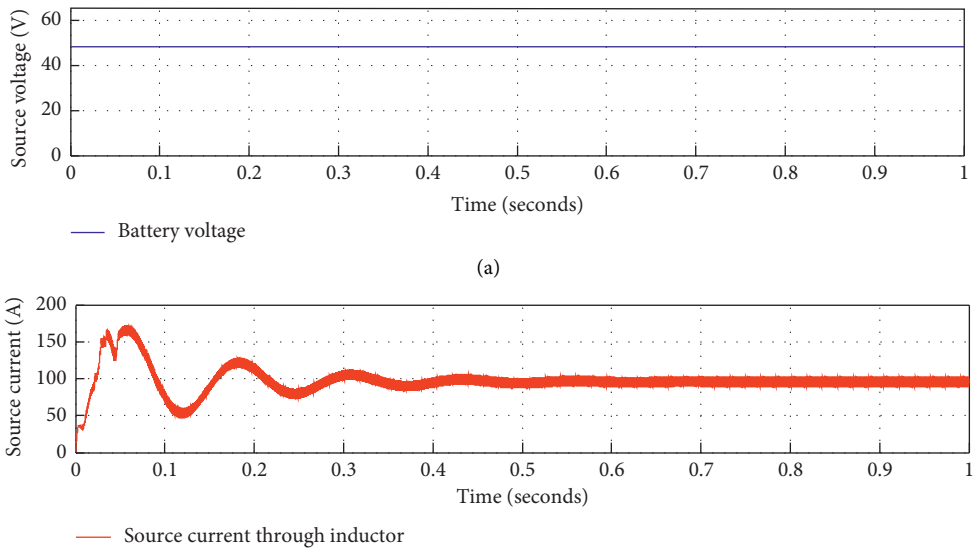

Figure 10: (a) Source voltage and (b) source current.

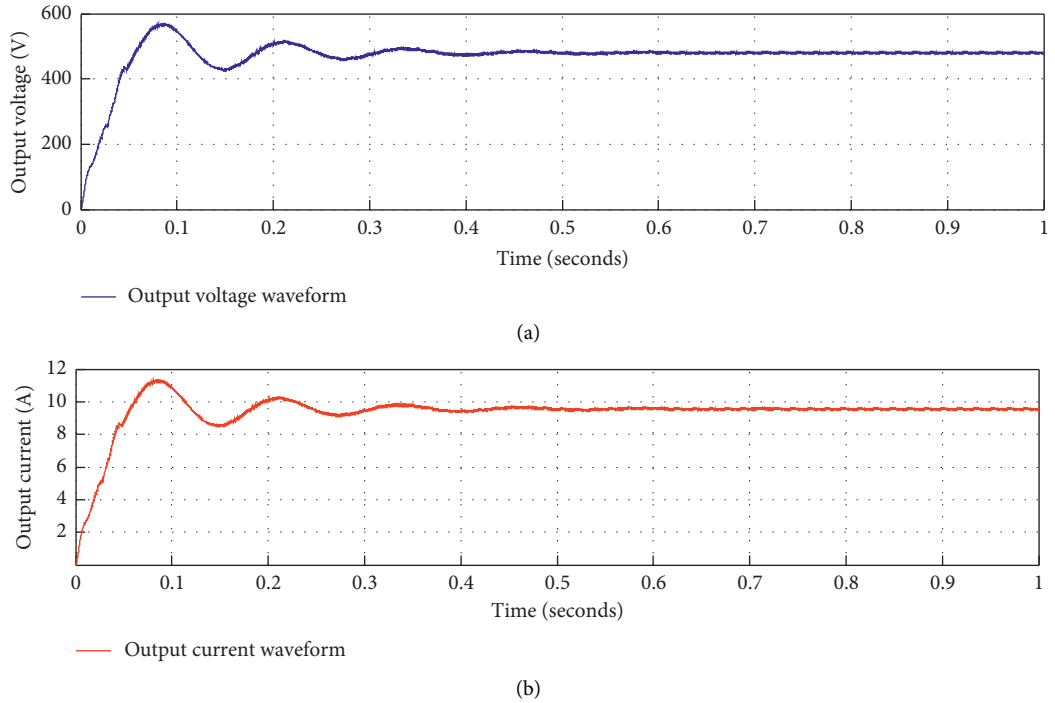

Figure 11: (a) Output voltage versus time and (b) output current versus time.

The spectral analysis of the output voltage realized in this work is portrayed in Figure 13. It is observed from the figure that the THD of the voltage output waveform obtained is 0.56% at 50 Hz fundamental frequency of the staircase reference signal.

The spectral analysis of the output power is shown in Figure 14. It can be observed from Figure 14 that the power output is 1.12% of the THD. This implies that the total current harmonics distortion is equal to 0.56%.

Figure 15 shows the tracking probability of output voltage waveform during transient and steady state on the normal statistical reference judgment. It was observed that during transient state, the output voltage waveform is beyond the judgment line with a probability value of

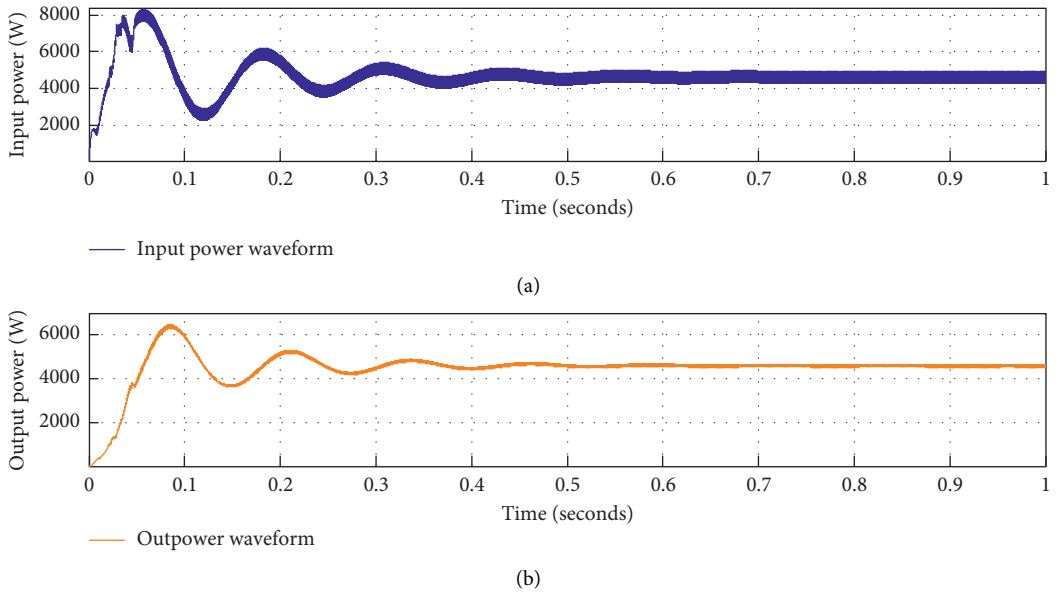

Figure 12: (a) Input power and (b) output power.

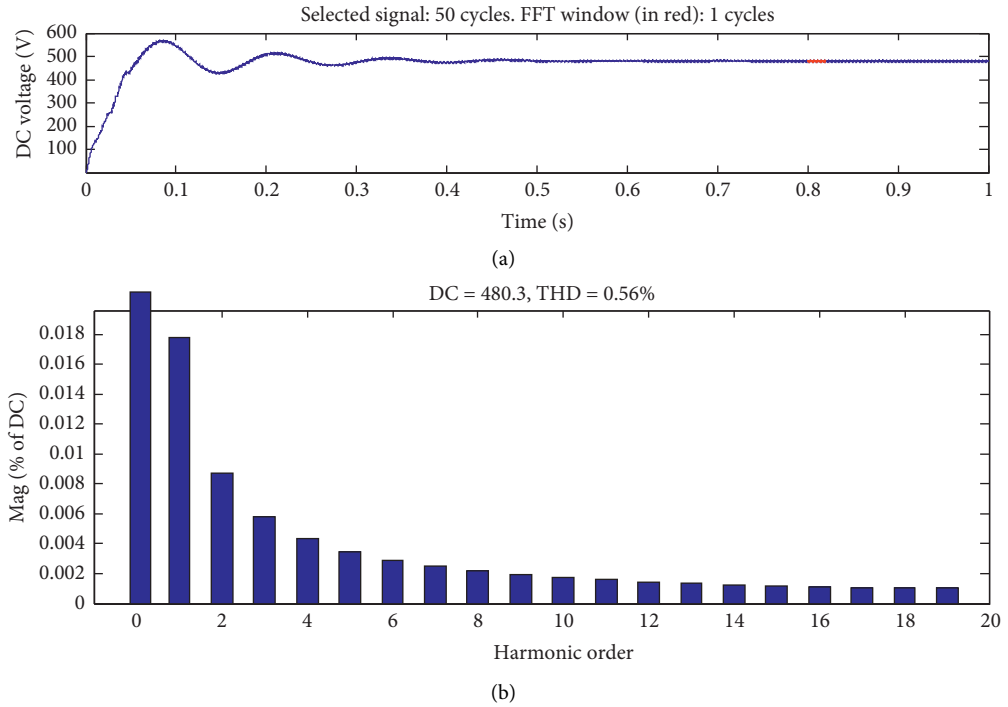

Figure 13: Spectral analysis of the output voltage.

0.12. This contributes relatively to high loss during the transient state. During the stable state, the probability of tracking is 0.90. This implies low power loss during the steady state.

A comparative analysis of different modulation schemes such as RTMS, DCVCSM, DCVTBM, and ZPCSMS, with the proposed scheme shown in Figure 2 is presented in Table 6. The comparison distinguishes the RTMS, DCVCSM, DCVTBM, and ZPCSMS schemes from the proposed scheme with respect to the nature of the firing signals, power input, power output, power losses, and THDs. Using the same criteria for all schemes, it was observed that the proposed scheme exhibits the lowest power loss as well as the highest power output and efficiency.

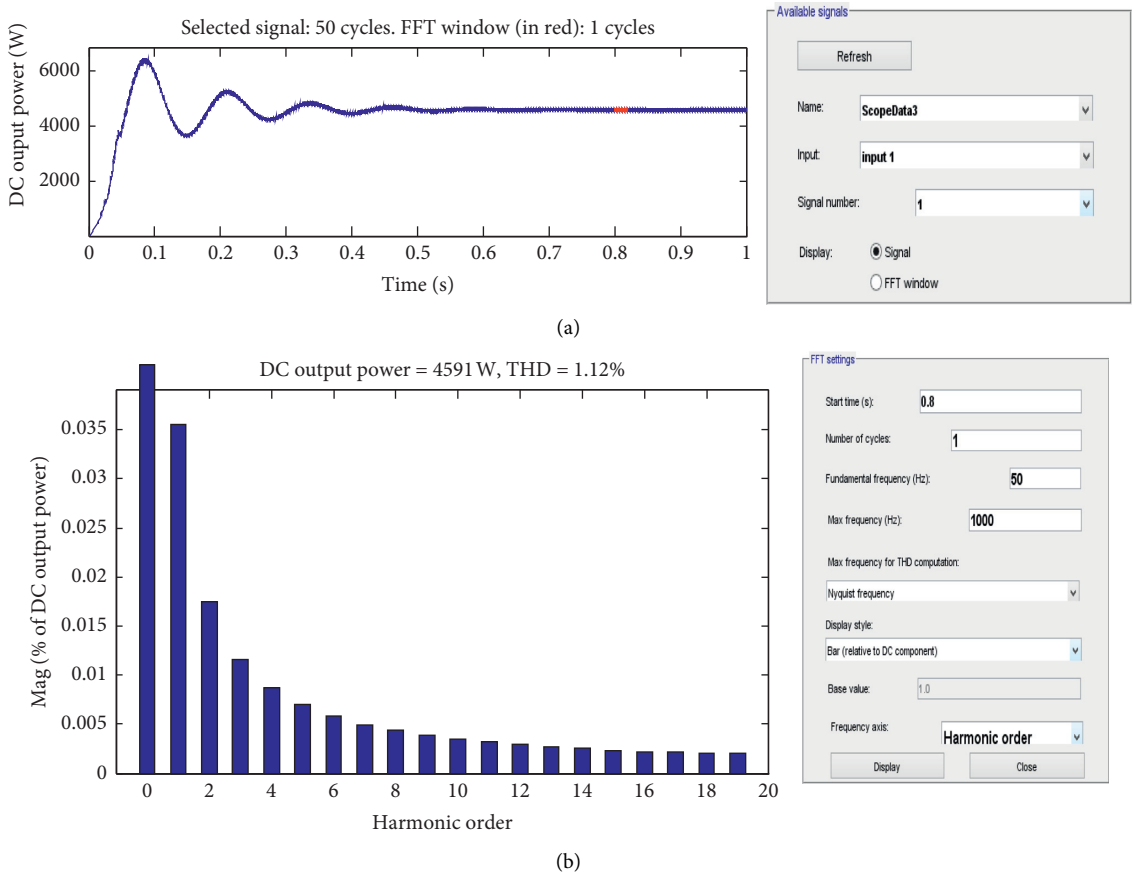

Figure 14: Spectral analysis of the output power.

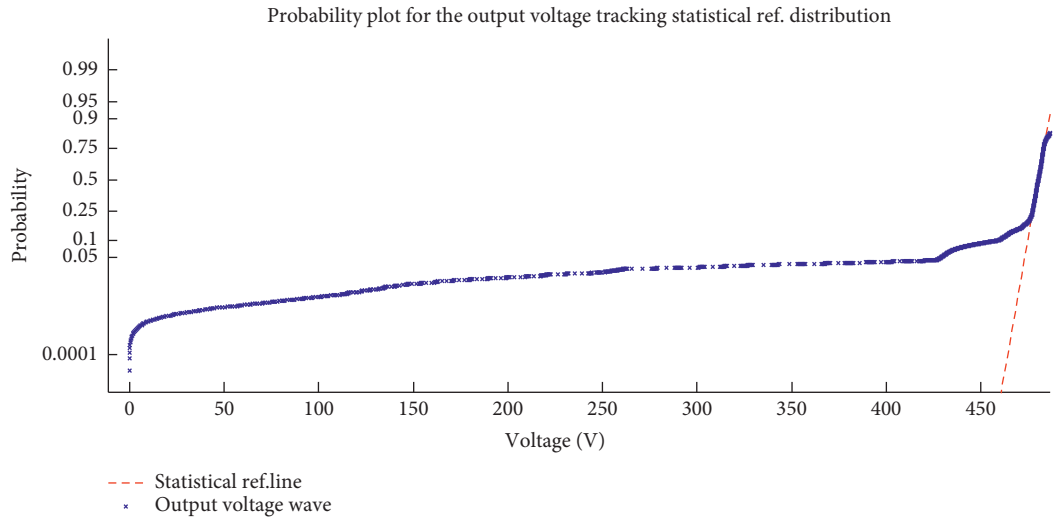

Figure 15: Output voltage versus statistical reference line.

Table 6 presents a comparison of conventional modulation schemes with the proposed scheme. The comparative analysis with existing schemes used in single switch boost DC-DC converters as shown in Figures 1, 3–5 as well as in Table 6, shows that the proposed nonzero staircase modulation scheme performs better than other conventional schemes.

Table 6: Comparative analysis of different modulation schemes.

Modulation scheme	Rectified-triangular modulation scheme (RTMS) Figures 1(a)–1(c) [13, 19]	DC voltage compared with Sawtooth modulation scheme (DCVCSM) Figures 3(a)–3(c) [12]	DC voltage-triangular based modulation scheme (DCVTBM) Figures 4(a)–4(c) [16–18]	Zero potential compared sinewave modulation scheme (ZPCSMS) Figures 5(a)–5(c) [13, 17]	Nonzero staircase modulation scheme (proposed scheme)
Nature of the firing signals	Irregular trains of pulses	Uniform trains of pulses	Uniform trains of pulses	Uniform trains of pulses	Two distinctive trains of pulses
System power input (W)	4800.00	4800.00	4800.00	4800.00	4800.00
System power output (W)	2928.00	4006.00	4204.00	2229.00	4591.00
System power losses (W)	1872.00	794.00	596.00	2571.00	209.00
System efficiency	66%	83%	88%	46%	96%
THD	9.79%	7.89%	4.65%	33.74%	1.12%

Apart from its outstanding performance, the proposed scheme also has a moderate impact during the transient state. Furthermore, we envisage that in real time implementation, it might require large operational amplifiers. This can be improved by using microcontroller-based nonzero staircase modulation schemes for practical purposes. The proposed modulation scheme can be applied in single switch or double switch boost DC-DC converter-based-hospital equipment such as in implantable cardiac pacemaker [26], oxygen concentrators, pulse oximeters, phototherapy device in rural healthcare centers, and ultrasound power supply units [27].

8. Conclusion

This paper presented a novel modulation scheme otherwise known as the nonzero staircase modulation scheme for switching single-switched DC-DC boost converter. The proposed scheme possesses the followings properties: power input of 4800 W, power output of 4591 W with 1.12% total harmonic distortion (THD), output voltage and current of 480.3 V and 9.56 A with 0.56% THD each, and efficiency of 96% and power loss of 209 W. The comparative analysis with existing schemes shows that the proposed scheme outperforms other existing modulation schemes.

Data Availability

All data sources have been appropriately cited within the manuscript.

Conflicts of Interest

The authors declare that they have no conflicts of interest.

References

[1] M. Forouzesh, Y. P. Siwakoti, S. A. Gorji, F. Blaabjerg, and B. Lehman, "Step-up DC-DC converters: a comprehensive review of voltage-boosting techniques, topologies, and applications," *IEEE Transactions on Power Electronics*, vol. 32, no. 12, pp. 9143–9178, 2017.

[2] D. W. Hart, *Power Electronics*, McGraw-Hill Companies, Inc., New York, NY, USA, 2011.

[3] M. H. Rashid, *Power Electronics Circuits, Devices and Application*, Prentice Hall of India, Delhi, India, Third edition, 2004.

[4] M. K. Kazimierczuk, *Pulse-Width Modulated DC-DC Power Converters*, Wiley, Chichester, UK, 2008.

[5] T. G. Wilson, "The evolution of power electronics," *IEEE Transactions on Power Electronics*, vol. 15, no. 3, pp. 439–446, 2000.

[6] B. Bose, "The past, present, and future of power electronics [Guest Introduction]," *IEEE Industrial Electronics Magazine*, vol. 3, no. 2, pp. 7–11, 2009.

[7] J. I. Leon, S. Kouro, L. G. Franquelo, J. Rodriguez, and B. Wu, "The essential role and the continuous evolution of modulation techniques for voltage-source inverters in the past, present, and future power electronics," *IEEE Transactions on Industrial Electronics*, vol. 63, no. 5, pp. 2688–2701, 2016.

[8] K. S. Srinivasu, S. M. Shariff, and K. Satyaanarayana, "Staircase control of hybrid multilevel inverter topology with reduced number of power electronic components," *International Journal of Scientific and Engineering Research*, vol. 7, pp. 865–872, 2016.

[9] N. R. Klaes and C. M. Ong, "Implementation and study of a digital staircase pulsewidth modulator," in *Proceedings of the IEEE Power Electronics Specialists Conference*, pp. 128–134, Blacksburg, VA, USA, June 1987.

[10] M. F. Mohammed, A. H. Ahmad, and A. T. Humod, "Efficiency improvement of DC-DC boost converter by parallel switches connection," *International Journal of Applied Engineering Research*, vol. 13, pp. 7033–7036, 2018.

[11] A. Tomaszuk and A. Krupa, "High efficiency high step-up DC/DC converters-a review," *Bulletin of the Polish Academy of Sciences: Technical Sciences*, vol. 59, no. 4, pp. 475–483, 2011.

[12] K. K. Tse, R. W.-M. Ng, H. S.-H. Chung, and S. Y. R. Hui, "An evaluation of the spectral characteristics of switching converters with chaotic carrier-frequency modulation," *IEEE Transactions On Industrial Electronics*, vol. 50, no. 1, pp. 171–182, 2003.

[13] M. U. Agu, *Principles of Power Electronics Circuits*, University of Nigeria Press, Enugu, Nigeria, 2019.

[14] R. Puviarasi, "SW-PWM for high power DC-DC boost converter in automotive fuel cell application," *International*

Journal of Pure and Applied Mathematics, vol. 119, no. 16, pp. 3903–3913, 2018.

[15] M. K. Kazimierczuk and L. A. Starman, "Dynamic performance of PWM DC-DC boost converter with input voltage feedforward control," *IEEE Transactions on Circuits and Systems I: Fundamental Theory and Applications*, vol. 46, no. 12, pp. 1473–1481, 1999.

[16] A. Fernández, J. Sebastián, P. Villegas, M. M. Hernando, and D. G. Lamar, "Dynamic limits of a power-factor preregulator," *IEEE Transactions on Industrial Electronics*, vol. 52, no. 1, pp. 77–87, 2005.

[17] H. D. Grahame and T. A. Lipo, "*Pulse Width Modulation for Power Converters," Principles and Practice*, Vol. 18, Wiley, Hoboken, NJ, USA, 2003.

[18] S. B. Santra, K. Bhattacharya, T. Roy Chudhury, and D. Chatterjee, "Generation of pulse width modulation schemes for power electronic converters," in *Proceedings of the National Power Systems Conference*, pp. 14–20, Tiruchirappalli, India, December 2018.

[19] C. I. Odeh, "Balancing switching losses in three-phase, five-level pulse-width modulation switched voltage source inverter using hybrid modulation techniques," *Electric Power Components and Systems*, vol. 42, pp. 1195–1200, 2014.

[20] J. M. Jacob, *"Industrial Control Electronics; Applications and Design"*, Prentice-Hall, Upper Saddle River, NJ, USA, 1989.

[21] A. Wahid and A. P. Prasetyo, "A comparative study between mpc and pi controller to control vacuum distillation unit for producing LVGO, MVGO, and HVGO," *IOP Conference Series: Materials Science and Engineering*, vol. 334, pp. 1–6, 2018.

[22] D. Chatterjee, "Voltage regulator using pi controller," Technical Report, National Institute of Technology, Tiruchirappalli, India, 2018.

[23] J. C. Basilio and S. R. Matos, "Design of PI and PID controllers with transient performance specification," *IEEE Transactions on Education*, vol. 45, no. 4, pp. 364–370, 2002.

[24] N. Farokhnia, H. Vadizadeh, S. H. Fathi, and F. Anvariasl, "Calculating the formula of line-voltage THD in multilevel inverter with unequal DC sources," *IEEE Transactions on Industrial Electronics*, vol. 58, no. 8, pp. 3359–3372, 2011.

[25] C. Eya and M. Agu, "Solar-based boost differential single phase inverter," *Nigerian Journal of Technology*, vol. 34, no. 1, pp. 164–176, 2015.

[26] M. K. Zaheeruddin and A. K. Sing, "Solar cell based boost converter for implantable cardiac pacemaker," *International Journal of Biomedical Engineering and Technology*, vol. 12, no. 3, 2016.

[27] H. Graham, T. Duck, D. Peel, R. Izadnegahdar, and C. Duke, "Solar powered healthcare," *International Journal of Tuberculosis and Lung Disease*, vol. 20, pp. 572-573, 2016.